

3 WILLMAN 1 REVISITED: THE KINEMATICS, CHEMISTRY, AND ORBITAL PROPERTIES OF A
4 POTENTIALLY-DISRUPTING DWARF GALAXY

5 CAMILLE CHIU¹, MARLA GEHA¹, WILLIAM CERNY¹, NITYA KALLIVAYALIL², HANNAH RICHSTEIN², CHRISTOPHER T. GARLING², AND BETH WILLMAN³

¹Department of Astronomy, Yale University, New Haven, CT 06520, USA

²Department of Astronomy, University of Virginia, Charlottesville, VA 22904, USA

³LSST Discovery Alliance, 933 North Cherry Avenue, Tucson, AZ 85719, USA

ABSTRACT

The ultra-faint Milky Way satellite Willman 1 (W1; $M_V = -2.5$; $r_{\text{half}} \sim 28$ pc) was the first stellar over-density found via resolved stars in the Sloan Digital Sky Survey, yet its classification as a dwarf galaxy or star cluster remains ambiguous. Based on new and improved Keck/DEIMOS spectroscopy, *HST/ACS* photometry, and orbital history, we re-examine the nature of W1. From our updated member sample of 57 stars, we find that past analyses included four binaries and eight clear non-members based on *Gaia* proper motions and updated velocities. We continue to find a velocity dispersion consistent with previous analyses, measuring $\sigma_v = 4.7^{+1.5}_{-1.3}$ km s⁻¹ from 49 stars out to $3r_{\text{half}}$. If W1 is in equilibrium, this suggests a dynamical mass of $\sim 5.9^{+3.8}_{-3.3} \times 10^5 M_\odot$ and mass-to-light ratio of $(M/L)_V = 660 \pm 600$. Based on Ca II triplet measurements, we estimate an iron-abundance of $[\text{Fe}/\text{H}] = -2.45^{+0.13}_{-0.13}$ and metallicity dispersion of $\sigma_{[\text{Fe}/\text{H}]} = 0.30^{+0.15}_{-0.11}$ dex. We confirm that W1 does not exhibit mass segregation inside of $\sim 1 r_{\text{half}}$. Our best-fit orbital model predicts that W1 is at the apocenter of its orbit, implying that W1 has been closer to the Milky Way in the recent past with a pericentric passage $\lesssim 25$ kpc from the Galactic center roughly 0.3 Gyr ago. Given its internal kinematics, metallicity spread, and lack of mass segregation, we conclude that W1 is a galaxy. However, based on its orbital solution and structural properties, which suggest that W1 might be tidally disrupted, and the difficulty in identifying a pure member sample, we caution that the measured internal velocity dispersion may not accurately reflect the dynamical mass of this system.

Keywords: Dwarf galaxies — Stellar kinematics — Milky Way dynamics

1. INTRODUCTION

The advent of wide-field photometric surveys such as the Sloan Digital Sky Survey (SDSS) and the Dark Energy Survey (DES) has led to the rapid discovery of several dozen Milky Way satellite galaxies, including populations of ultra-faint dwarf galaxies and ultra-faint star clusters (e.g., Willman et al. 2005; Belokurov et al. 2007; Drlica-Wagner et al. 2015; Koposov et al. 2015; Torrealba et al. 2016; Homma et al. 2024; Cerny et al. 2024). The faintest and most compact of these stellar systems, with stellar masses of only a few hundred solar masses and half-light radii of only tens of parsecs, blur the line between globular clusters and dwarf galaxies (e.g., Smith et al. 2024). The classification of an object as a dwarf galaxy or star cluster typically hinges on one or both of the following diagnostics (Willman & Strader 2012): (1) a kinematic distribution that cannot be explained solely by its baryonic component, implying the presence of large quantities of dark matter; (2) a spectroscopically observed spread in [Fe/H] metallicity, indicating multiple epochs of star formation. Beyond these two criteria, the presence of mass segregation has also been used as a discriminator (Baumgardt

²⁸ et al. 2022).

Willman 1 (W1; SDSSJ1049+5103) was first identified as an over-density of old, metal-poor stars in SDSS DR2 by Willman et al. (2005), becoming the first ultra-faint Milky Way companion discovered in SDSS. Despite tentative evidence for mass segregation, Willman et al. (2006) initially leaned towards a dwarf galaxy classification for W1 based on an observed metallicity spread between three red giant branch (RGB) stars. This classification was supported by Keck/DEIMOS spectroscopy by Martin et al. (2007), who identified 7 RGB members with a significant metallicity spread. However, follow-up spectroscopy from the Hobby-Eberly Telescope by Siegel et al. (2008) determined that at least 2 and up to 5 of these identified RGB stars were likely Milky Way foreground dwarf stars, significantly decreasing the observed metallicity spread. From a reanalysis with Keck/DEIMOS spectroscopy and a careful characterization of foreground contamination, Willman et al. (2011) identified 45 member stars, 40 of which were classified as high confidence. This included an additional RGB member and two HB members whose metallicity spread was once again indicative of a dwarf galaxy. These spectroscopic re-

sults are confirmed by the photometric *HST*-based metallicity distribution function measured by Fu et al. (2023), who determined a significant metallicity spread of $\sigma_{\text{[Fe/H]}} = 0.65^{+0.10}_{-0.09}$ dex. At the time of discovery, W1 was the lowest luminosity galaxy known ($M_V = -2.5$; Willman et al. 2005).

Assuming equilibrium, Willman et al. (2011) estimated a dynamical mass of $\sim 3.9 \times 10^5 M_\odot$ based on a velocity dispersion of $4.8 \pm 0.8 \text{ km s}^{-1}$, implying a mass-to-light (M/L) ratio of ~ 770 . Due to this apparent high dark matter content and relatively close proximity at a distance of ~ 38 kpc, W1 continues to be an attractive target in the search for dark matter annihilation signals in gamma rays (e.g., Aliu et al. 2009; Bringmann et al. 2009; Li et al. 2021; McDaniel et al. 2023) and X-rays (e.g., Nieto & Mirabal 2010; Loewenstein & Kusenko 2010, 2012; Saeedi & Sasaki 2020).

Yet, previous studies of W1 found evidence for stellar multi-directional tails and a tentative excess of stars at large half-light radii (Willman et al. 2006, 2011). Specifically, Willman et al. (2011) reported an irregular kinematic distribution where stars within the effective half-light radius have a systematically higher velocity than those beyond; this possibly disturbed morphology might point to tidal interactions. If W1 is not in dynamical equilibrium and indeed is tidally disrupted, then the dynamical mass inferred from its internal velocity dispersion may be misleading.

The main difficulty in accurately classifying W1 and determining its properties lies in the kinematic and spectroscopic similarities between the foreground stars in the Milky Way and the members of W1 (Siegel et al. 2008; Willman et al. 2011; Saeedi & Sasaki 2020). With an estimated systemic radial velocity of $-12.8 \pm 1.0 \text{ km s}^{-1}$, the velocities of W1 stars heavily overlap with the velocities of Milky Way stars (Willman et al. 2011). If W1 is tidally disrupted, spatial and kinematic cuts, which are often implemented to supplement photometric color-magnitude (CMD) cuts, might instead obscure the odd structural and kinematic features of W1. On the other hand, due to the already small sample size of stars, just a few Milky Way contaminants in the member sample could artificially inflate the velocity dispersion, and thus the inferred dynamical mass of W1, as well as the metallicity spread that is used to characterize it as a dwarf galaxy in the first place.

To address these uncertainties, this paper revisits W1 and presents a comprehensive study of its structural, kinematic, chemical, and orbital properties. First, we present a uniform analysis of both new and archival Keck/DEIMOS spectroscopy for W1 and *Gaia* astrometry (§2). We discuss the probabilistic membership selection performed to reduce the presence of Milky Way foreground contamination (§3). From this member sample, we measure the properties of W1 including its velocity dispersion, inferred dynamical mass, and metallicity distribution (§4). With *HST*/ACS imaging of W1, we summarize previous results for W1’s star formation history and look for evidence for mass segregation (§5). We

next model the dynamical history of W1, including its orbit and mock tidal streams (§6). We conclude with a discussion of W1’s classification as either a dwarf galaxy or star cluster and its tidal disruption status (§7).

2. OBSERVATIONS AND DATA REDUCTION

Our kinematic analysis is based on a homogeneous reduction of archival Keck/DEIMOS spectroscopic data (§2.1, §2.1.1, §2.2), half of which is published here for the first time. We supplement this with ground-based photometry and *Gaia* astrometry (§2.3).

2.1. Keck/DEIMOS Spectroscopy: Kinematics

We present homogeneously reduced archival data of W1 from the DEIMOS spectrograph (Faber et al. 2003) on the Keck II 10-m telescope. Twelve multislit masks were taken of W1 between 2006–2023 (see Table 1). One of these masks was first presented in Martin et al. (PI: Chapman 2007) and four masks were published in Willman et al. (PI: Brodie 2011). The remaining seven masks are presented here for the first time [PIs: Geha, Rich]. All data were taken with the 1200G grating, providing a spectral resolving power of $R \sim 6000$ at 8500\AA . The spectral dispersion of this setup is roughly 0.33 \AA per pixel with a resulting spectral resolution of 1.37 \AA (FWHM). A summary of observations is presented in Table 1.

A detailed discussion of the data reduction is presented in Geha et al. (2026) and briefly discussed here. Raw science frames and associated calibrations were obtained through the Keck Observatory Archive¹. Data were reduced to one dimensional wavelength-calibrated spectra using the open-source python-based data reduction code PypeIt (Prochaska et al. 2020). PypeIt reduces the eight individual DEIMOS detectors as four mosaic images, where each red/blue pair of detectors is reduced together.

Stellar radial velocities were measured using the dmost package (Geha et al. 2026)². dmost first pre-processes spectra to identify and remove extragalactic objects using a modified version of the automated redshift software Marz (Hinton et al. 2016). For the remaining spectra, dmost forward models the 1D spectrum for each source from a given exposure with both a stellar template from the PHOENIX library (Husser et al. 2013) and a synthetic telluric absorption spectrum from TelFit (Gullikson et al. 2014). The velocity is determined for each science exposure through an MCMC procedure constraining both the radial velocity of the target star as well as a wavelength shift of the telluric spectrum needed to correct for slit miscentering (see, e.g., Sohn et al. 2007). We reject velocities where the posterior shape is far from Gaussian, largely spectra with $S/N < 3$. The final radial

¹ <https://koa.ipac.caltech.edu>

² <https://github.com/marlageha/dmost>

velocity for each star is derived through an inverse-variance weighted average of the velocity measurements from each individual exposure. In cases where less than half of individual science exposures for a given star produce a reliable velocity measurement, we attempt to measure a velocity based on the 1D coadded spectrum following the same method above. In both cases, a velocity error scaling and velocity floor is applied to the random errors, based on an assessment from thousands of repeat DEIMOS measurements as discussed in Geha et al. (2026). The velocity error floor is 1.1 km s^{-1} for a velocity measured on a single mask.

There are 474 unique targets with extracted DEIMOS spectra, plus 28 sources extracted serendipitously in addition to the target source. We have photometry and were able to measure radial velocities for 340 of these sources. 125 of these sources are extra-galactic, including 14 broad-line quasar spectra. The remaining 215 sources have velocities and spectra consistent with stars, although we expect only a fraction of these to be W1 members (see §3.1). 12 of these sources have velocity uncertainties greater than 15 km s^{-1} , above the threshold considered as a secure velocity measurement by Geha et al. (2026), and are thus not considered for membership. We therefore consider 203 stars with measured ra-

dial velocities for membership. The radial velocities for the 203 stars and redshifts for the 125 extragalactic sources are available in Table 4 and 5 of Geha et al. (2026), respectively.

2.1.1. Flagging Velocity Variables

To identify velocity variables, we evaluate whether or not velocities measured at different times are consistent with random fluctuations from a constant value. For each star, we first calculate the weighted mean velocity, the equivalent of assuming a constant velocity model. We then calculate the χ^2 value for this model, including random and systematic error components. Following Maxted et al. (2001), we then calculate the probability, p , of obtaining the observed value of χ^2 or higher from random fluctuations around a constant value. p is evaluated for the appropriate number of degrees of freedom (the number of observations minus one). We define a star as a velocity variable if $\log_{10} p < -1$. 63 out of 341 stars have velocities measured on multiple DEIMOS mask pointings, all of which have measurements separated by more than one year. We find 16 of these stars to be velocity variables, 6 of which are members. Their positions on the CMD are shown in Figure 1a.

Table 1. Summary of Willman 1 Keck/DEIMOS Observations.

Mask	Date	N_{exp}	Σt_{exp} (sec)	PIs	Slit width (arcsec)	N_{slits}	$N_{\text{good}}/N_{\text{slits}}$	Reference
203WiSB	20060527	3	3600	Chapman	0.7	63	0.62	Martin et al. (2007)
W1_1	20061120	5	9000	Brodie	1	113	0.48	Willman et al. (2011)
W1_2	20061121	5	9000	Brodie	1	101	0.38	Willman et al. (2011)
W1_3	20061122	3	5400	Brodie	1	92	0.41	Willman et al. (2011)
W1_4	20070320	3	5400	Brodie	0.7	123	0.07	Willman et al. (2011)
W1_5	20170425	7	12000	Geha	0.7	71	0.28	New Data; this work
W1_6	20170426	5	9000	Geha	0.7	66	0.42	New Data; this work
W1_9	20210408	5	9000	Geha	0.7	70	0.4	New Data; this work
Wil1_1B	20230124	6	7200	Rich	0.8	39	0.38	New Data; this work
wil1_5	20230124	6	7200	Rich	0.8	33	0.45	New Data; this work
Wil1_2B	20230125	6	7200	Rich	0.8	31	0.42	New Data; this work
wil1_6	20230125	6	7200	Rich	0.8	29	0.34	New Data; this work

Note—List of DEIMOS masks present in this work. (1) DEIMOS mask name, (2) date observed, (3) number of exposures reduced in this work, (4) total integrated exposure time, (5) Principal Investigator (PI) name, (6) slit width, (7) number of slits in a mask, (8) fraction of targeted objects in a mask with a measured velocity, (9) Published reference.

2.2. Keck/DEIMOS Spectroscopy: Metallicities

We use dmst to measure the equivalent width of several stellar absorption lines. We first determine equivalent widths for NaI: $\lambda 8183, 8185 \text{\AA}$ and MgI: $\lambda 8807 \text{\AA}$. The strengths of the NaI and MgI lines are used as proxies for surface gravity to evaluate membership in W1. We model these lines as

a double or single Gaussian, respectively, and integrate the resulting fitted parameters to determine equivalent widths. These quantities are used at the end of §3.1 to validate membership selection.

We measure the equivalent width of the Ca II triplet (CaT) lines ($\lambda 8498, 8542, 8662 \text{\AA}$) as described in Geha et al.

(2026). We simultaneously model the three Ca II triplet lines with a Gaussian-plus-Lorentzian profile (for stars at S/N > 15 per spectral pixel) or a Gaussian profile (for stars at S/N < 15 per spectral pixel). We integrate the resulting fits to determine total equivalent width, which we refer to as CaT. From these CaT EW measurements, we derived [Fe/H] measurements for all candidate RGB stars ($M_V < 3$) assuming the empirical luminosity-dependent EW-[Fe/H] calibration from Navabi et al. (2026) which is an update to the Carrera et al. (2013) calibration using the same functional form. We adopted the form of the calibration based on the absolute V -band magnitude of each star, which we estimated by transforming our MegaCam g - and r -band photometry (see §2.3). As detailed in Geha et al. (2026), an error floor of 0.05Å is added to the CaT measurements based on repeat measurements, while a 0.1 dex error floor is included in the [Fe/H] values to account for inherent scatter in the Carrera et al. calibration itself, noting this term dominates at S/N > 25.

2.3. Ground-based Imaging and Matching to Gaia

We require photometry for all kinematic measurements to assess membership in W1 (see Figure 2, top panel). We use the Canada-France-Hawaii Telescopes (CFHT) MegaCam photometric catalog from Muñoz et al. (2018a) and adopt the fitted density profile and structural parameters from this analysis (see Table 2). These data are a full magnitude deeper than that available from the DESI Legacy Imaging Surveys DR9 (Dey et al. 2019). The Muñoz et al. (2018a) g - and r -band magnitudes are corrected for foreground Galactic extinction using Schlegel et al. (1998). Given the small magnitude uncertainties reported by Muñoz et al. (2018a) (< 0.01 mag), we add a systematic photometric uncertainty of 0.02 mag in quadrature.

A important improvement to previous studies of W1 is the available *Gaia* DR3 catalogue (Gaia Collaboration et al. 2023). While *Gaia* will only cover W1 stars above the sub-giant branch ($r \lesssim 20$), it significantly reduces contamination in this region due to the addition of proper motion and parallax measurements. We match our DEIMOS catalog to *Gaia* DR3 with a 1'' matching radius, resulting in 65 matches that are considered for membership.

3. MEMBERSHIP SAMPLE

Assessing whether a given star belongs to W1 or is part of the foreground Milky Way is particularly challenging because of the kinematic overlap between these two populations. We begin by describing our membership assessment method (§3.1). We then present our final member sample and compare to previous member samples in the literature (§3.2).

3.1. Membership Determination

To evaluate the likelihood that a given star is a member of W1, we assess five criteria for membership: (1) the star's position on the color-magnitude diagram (CMD), P_{CMD} ; (2) the

star's heliocentric radial velocity, P_{vel} ; (3) the star's proper motion, P_{pm} ; (4) the star's parallax, P_{parallax} ; and (5) the star's [Fe/H] iron abundance, $P_{[\text{Fe}/\text{H}]}$. Criteria (3) and (4) are only considered for stars with parallax and proper motion measurements available from *Gaia* DR3 (Gaia Collaboration et al. 2023, see §2.3).

Due to tentative evidence for multi-directional tails and tidal stripping (Martin et al. 2007; Willman et al. 2011), no spatial cuts were performed on the data as to not introduce assumptions about W1's spatial spread of stars, although we limit our sample to $3r_{\text{half,ell}}$ to determine physical properties (see §4). We additionally consider two surface gravity indicators (NaI and MgI), but find these do not improve membership discrimination for the case of W1 and discuss this below. The membership probability, P_{mem} , of a star is defined as the product of all five criteria (Figure 1):

$$P_{\text{mem}} \propto P_{\text{CMD}} \times P_{\text{vel}} \times P_{\text{pm}} \times P_{\text{parallax}} \times P_{[\text{Fe}/\text{H}]} \quad (1)$$

We next describe in more detail each of the terms above.

P_{CMD} is determined by comparing each star's position on the color-magnitude diagram to an old, metal-poor isochrone from the PARSEC stellar evolutionary track models ($\tau = 12$ Gyr, Fe/H = -2.1, Bressan et al. 2012). We use the updated distance value of 38.55 ± 0.45 based on *HST* imaging from Durbin et al. (2025, uncertainty via private communication). This value is consistent with that measured in Willman et al. (2011, 38 ± 7 kpc). We use this to calculate the minimum distance between the isochrone and the star's location on the CMD. This distance (d_{\min}) and the overall magnitude uncertainty of the star (δ_{mag} , the quadrature sum of the r -band and g -band magnitude uncertainty), are then used to evaluate the star's CMD membership probability, P_{CMD} (see Figure 1a):

$$P_{\text{CMD}} = \exp\left(-\frac{d_{\min}^2}{2[\sigma_{\text{CMD}}^2 + \delta_{\text{mag}}^2]}\right), \quad (2)$$

where σ_{CMD} is set to 0.15 mag. This CMD spread was roughly estimated from the span of other possible isochrones with varying ages and metallicities ($\tau = 8$ to 13 Gyr, [Fe/H] = -1.9 to -2.3) to account for the uncertainty in both parameters.

P_{vel} is based on each star's heliocentric, line-of-sight velocity and, for consistency's sake, is calculated using a similar probability distribution as P_{CMD} . For a star with velocity $v \pm \delta_v$, its membership probability based on velocity, P_{vel} , is calculated as (see Figure 1b):

$$P_{\text{vel}} = \exp\left(-\frac{(v - v_{W1})^2}{2[(3\sigma_v)^2 + \delta_v^2]}\right), \quad (3)$$

where $v_{W1} = -12.8 \text{ km s}^{-1}$, the systemic velocity of W1, and $\sigma_v = 4.8 \text{ km s}^{-1}$, the velocity dispersion of W1, as determined by Willman et al. (2011). We multiply the velocity dispersion by three to loosen the distribution and avoid artificially biasing the sample towards the priors.

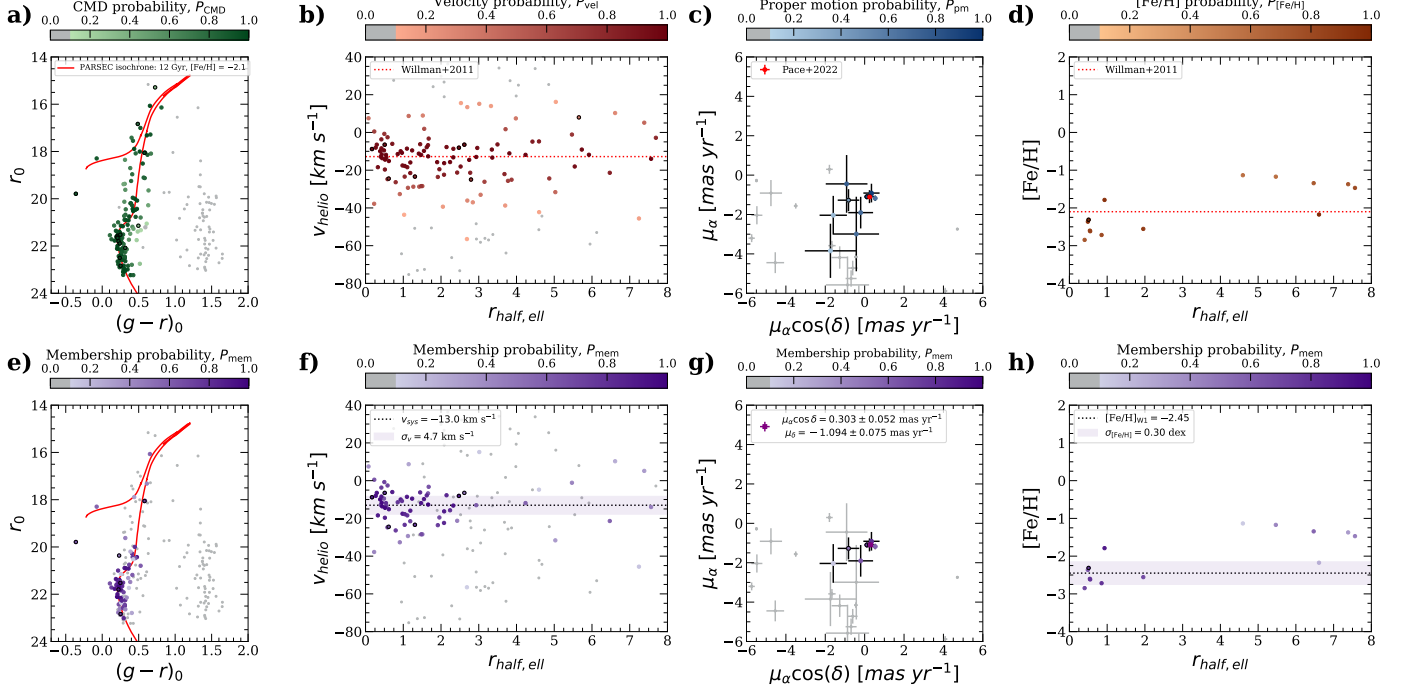


Figure 1: From our five criteria for membership (*a, b, c, d*), the membership probability of each star was determined (*e, f, g, h*). In each plot (*left to right*: CMD, velocity, proper motion, and metallicity profile), all stars with photometric and radial velocity measurements are color-coded according to the membership probability of the criterion in question, with clear non-members ($P_{\text{criterion}} < 0.1$) colored gray. Stars with variable velocities are circled in black. The priors for each marker are delineated in the top panels (Willman et al. 2011; Pace et al. 2022), and the properties derived from our member sample are shown in the bottom panels (see §4, Table 2).

For stars with measured *Gaia* proper motions and parallaxes, the corresponding membership probabilities for each of these quantities, P_{pm} and P_{parallax} , were determined. Pace et al. (2022) report proper motion values of $(\mu_{\alpha}^*, \mu_{\delta}) = (0.255 \pm 0.085, -1.110 \pm 0.096)$ mas yr⁻¹ for W1 based on *Gaia* EDR3 astrometry. For a star with proper motion $(\mu_{\alpha}^*, \mu_{\delta})$ and overall proper motion uncertainty δ_{pm} (calculated by summing the two dimensions in quadrature), the membership probability based on proper motion, P_{pm} , is defined as (see Figure 1c):

$$P_{\text{pm}} = \exp\left(-\frac{(\mu_{\alpha}^* - \mu_{\alpha,W1}^*)^2 + (\mu_{\delta} - \mu_{\delta,W1})^2}{2[(2\sigma_{\text{pm}})^2 + \delta_{\text{pm}}^2]}\right), \quad (4)$$

where σ_{pm} is the reported Pace et al. (2022) proper motion uncertainties added in quadrature. Stars with a proper motion uncertainty more than twice its signal value are treated as non-measurements.

Situated at a distance of ~ 39 kpc, the parallax of W1 is immeasurable by *Gaia*. As we find that the proper motion membership criteria cleans the sample for the brightest stars, we opt for a simple binary parallax marker: The parallax membership probability is defined as $P_{\text{parallax}} = 1$ for stars with parallax-over-error is less than 3 and $P_{\text{parallax}} = 0$ for stars with parallax-over-error is greater than 3.

Finally, $P_{[\text{Fe}/\text{H}]}$ is determined from the CaT-based metallicity, $[\text{Fe}/\text{H}]$, for each star. Similar to the other markers, we determine the metallicity membership probability for a star with iron abundance $[\text{Fe}/\text{H}] \pm \delta_{[\text{Fe}/\text{H}]}$ as (see Figure 1d):

$$P_{[\text{Fe}/\text{H}]} = \exp\left(-\frac{([\text{Fe}/\text{H}] - [\text{Fe}/\text{H}]_{W1})^2}{2[(2\sigma_{[\text{Fe}/\text{H}]}))^2 + \delta_{[\text{Fe}/\text{H}]}^2]}\right), \quad (5)$$

where $[\text{Fe}/\text{H}]_{W1} = -2.1$, the mean spectroscopic metallicity of W1, and $\sigma_{[\text{Fe}/\text{H}]} = 0.45$ dex, half the distance between the most metal-poor and metal-rich star in the three star spectroscopic sample of Willman et al. (2011). This measurement was chosen as our prior as it is the largest member sample available with spectroscopic metallicity measurements.

Beyond these five parameters, there are a few spectral lines covered by DEIMOS that can be incorporated into membership selection to further differentiate between member stars and Milky Way dwarf star contaminants. The NaI absorption line at 8234 Å correlates with surface gravity and can be used to identify Milky Way dwarf stars which display systematically stronger lines than giants (Schiavon et al. 1997). All stars with $P_{\text{mem}} > 0.5$ have small NaI equivalent widths (< 1 Å within $1-\sigma$). Battaglia & Starkenburg (2012) identified a distinction line between RGB stars and dwarf stars in the equivalent width of the MgI line at 8806.8 Å as a function of the equivalent width of the Calcium II triplet lines

that can also be used to cut Milky Way dwarf star interlopers. All stars with $P_{\text{mem}} > 0.5$ lie within $1-\sigma$ of the cut-off line, a result that is consistent with the predictions for a metal-poor system. While the use of these NaI and MgII lines are somewhat redundant and do not add more layers to our membership selection, they are a useful tool for validating that our selection criterion are efficiently differentiating between W1 members and Milky Way foreground stars.

3.2. Final Member Sample and Comparison to Literature Samples

The membership probability, P_{mem} , of each star is shown in the bottom panels of Figure 1. From this, we define stars with $P_{\text{mem}} > 0.5$ as members of W1. This results in 57 members, all but 1 of which lie within $3 r_{\text{half,ell}}$. We recognize the subjectiveness of this probability cut-off and take this into account when calculating the properties of W1 (see §4.1). Multiple velocity epochs exist for 36 of the 57 stars in our sample, from which we identify 6 velocity variables, including 1 blue straggler. We infer the physical parameters of W1 from the 49 members within $3 r_{\text{half,ell}}$, and these properties are presented in Table 2.

As shown in Figure 2, we report that 28 members are inside the elliptical half-light radius, 19 of which have multiple velocity epochs and non-variable velocities. We highlight that, despite implementing no spatial cuts, the stellar density distribution of our member sample shows no stars in excess of a Plummer profile assuming completeness. The CMD of W1 members is consistent with that of an old, metal-poor system, and we identify 8 RGB stars for which we measure spectroscopic metallicities.

All 45 published members in Willman et al. (2011) overlap with the Keck/DEIMOS spectroscopy within $1.5''$. Due to more stringent quality criteria, six stars in the 2011 sample have no velocity measurements in this work due to low S/N and poor velocity fits and were thus not considered for membership. A total of 31 stars in the 2011 sample overlap with the 57 member stars in this work. The eight remaining stars in the 2011 sample are labeled as non-members: four on the basis of proper motion/parallax estimates from Gaia, three due to updated velocities that are inconsistent with the systemic motion of W1, and one due to its large velocity uncertainty that did not pass quality cuts. We also find the presence of four stars flagged as velocity variables by this work in the 2011 sample. Of the 52 foreground Milky Way stars reported in Willman et al. (2011), 51 stars have matches with our measured velocities. One of these stars is included in our member sample based on an updated velocity measurement, and the rest are confirmed as non-members by this work.

The completeness of our kinematic sample was evaluated by comparing with the CFHT MegaCam photometric catalog from Muñoz et al. (2018a). This photometric catalog was restricted to stars within $3 r_{\text{half,ell}}$ and $P_{\text{CMD}} \geq 0.5$, ensuring that we only evaluate the completeness of our sample against

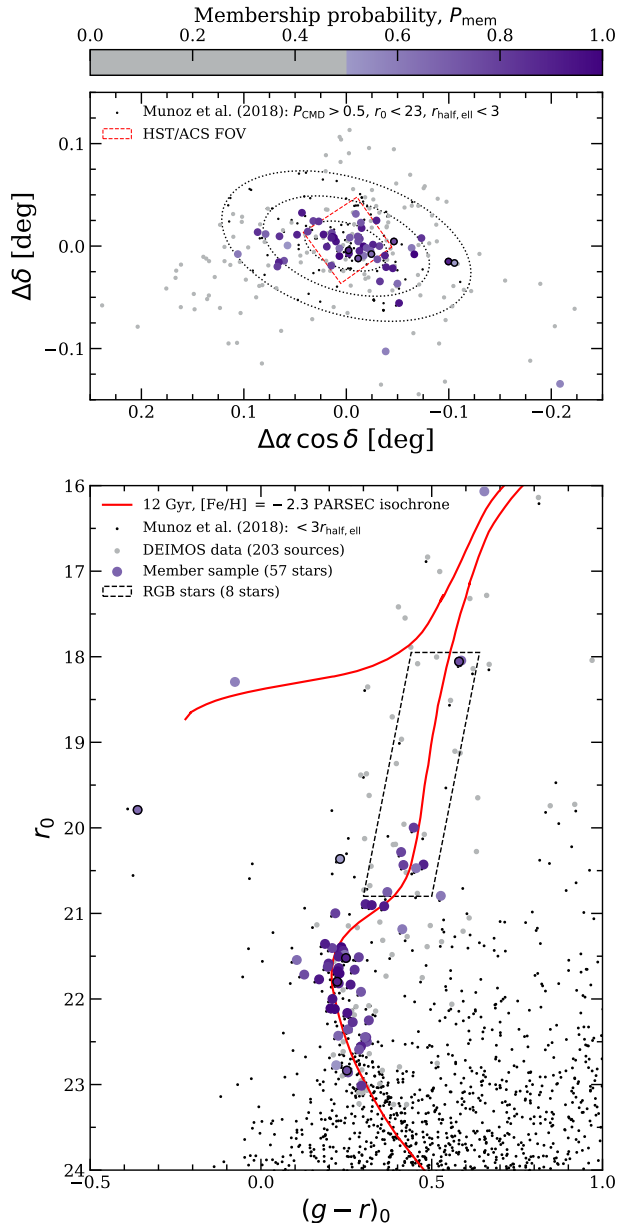


Figure 2: *Upper:* Spatial distribution of the 57 W1 member stars, color-coded according to P_{mem} . Members with variable velocities are circled in black and non-members are in colored gray. The three concentric dotted ellipses represent the space within 1, 2, and 3 $r_{\text{half,ell}}$. All stars with photometry from Muñoz et al. (2018a) within $3 r_{\text{half,ell}}$, $P_{\text{CMD}} > 0.5$, and $r_0 < 23$ are shown in black. The field of view of the HST/ACS imaging is denoted red (see §5.1). *Lower:* Color-magnitude diagram of W1 member stars overlaid with an old, metal-poor PARSEC isochrone in red. All stars with photometry from Muñoz et al. (2018a) within $3 r_{\text{half,ell}}$ are shown in black. The liberally defined red giant branch for which we measure spectroscopic metallicities is boxed.

likely member stars (see Figure 2). All stars with $r_0 \leq 21$ inside 1 half-light radius have spectroscopic measurements

and are included in our analysis. For fainter stars ($r_0 \leq 23$), the spectroscopic completeness decreases approximately linearly from 100% to 70% from 0 to $3 r_{\text{half,ell}}$.

Table 2. Properties of Willman 1.

Parameter	Value	Units	Reference
α_{J2000}	162.3436	deg	Muñoz et al. (2018a)
δ_{J2000}	51.0501	deg	Muñoz et al. (2018a)
D_\odot	38.55 ± 0.45	kpc	Durbin et al. (2025) ^a
$(m - M)_0$	17.93 ± 0.03	mag	Durbin et al. (2025) ^a
r_{half}	2.51 ± 0.22	arcmin	Muñoz et al. (2018b)
r_{half}	26.8 ± 3.2	pc	Muñoz et al. (2018b)
ϵ	0.47	—	Muñoz et al. (2018b)
Position angle	73	deg	Muñoz et al. (2018b)
M_V	-2.56 ± 0.74	mag	Muñoz et al. (2018b)
L_V	888 ± 605	$L_{V,\odot}$	Muñoz et al. (2018b)
v_{sys}	$-13.0^{+1.1}_{-1.1}$	km s^{-1}	§4.1
σ_v	$4.7^{+1.5}_{-1.3}$	km s^{-1}	§4.1 ^b
$M_{1/2}$	$\sim 5.9^{+3.8}_{-3.3} \times 10^5$	M_\odot	§4.1
$(M/L)_{V,1/2}$	660 ± 600	$M_\odot / L_{V,\odot}$	§4.1
[Fe/H]	$-2.45^{+0.13}_{-0.13}$	—	§4.2
$\sigma_{\text{[Fe/H]}}$	$0.30^{+0.15}_{-0.11}$	dex	§4.2
μ_a^*	0.303 ± 0.052	mas yr^{-1}	§6.1
μ_δ	-1.094 ± 0.075	mas yr^{-1}	§6.1
r_{peri}	$14.8^{+1.9}_{-1.6}$	kpc	§6.1 ^c
r_{apo}	$43.2^{+0.5}_{-0.5}$	kpc	§6.1 ^c
e	$0.49^{+0.04}_{-0.05}$	—	§6.1 ^c

NOTE—List of global structural, kinematic, chemical, and orbital parameters of W1.

^aThe reported distance/distance modulus uncertainty is likely underestimated as it does not include the systematic contributions from isochrones.

^bWe opt to cite the velocity dispersion determined from our two-component Gaussian mixture model as it incorporates the uncertainty in membership.

^cWe report the orbital properties determined from MWPotential2014 of Bovy (2015), with the dark matter halo mass scaled up by 50% and the addition of the LMC.

4. RESULTS

With a sample of 49 W1 members within $3 r_{\text{half,ell}}$ with measured velocities, we next probe the **kinematic** (§4.1) and **chemical** (§4.2) properties of this system.

4.1. Velocity Dispersion and Dynamical Mass

Based on our member sample, we present the velocity profile of W1 in Figure 3. Willman et al. (2011) reported a peculiar velocity profile where stars within $\sim 0.75 r_{\text{half,ell}}$ are offset from those at the outskirts. This phenomenon is still observed by eye in our updated member sample (see Figure 3, upper panel). Quantitatively, the rolling average decreases by about $8.5 \pm 3.0 \text{ km s}^{-1}$ from the center to the outskirts of

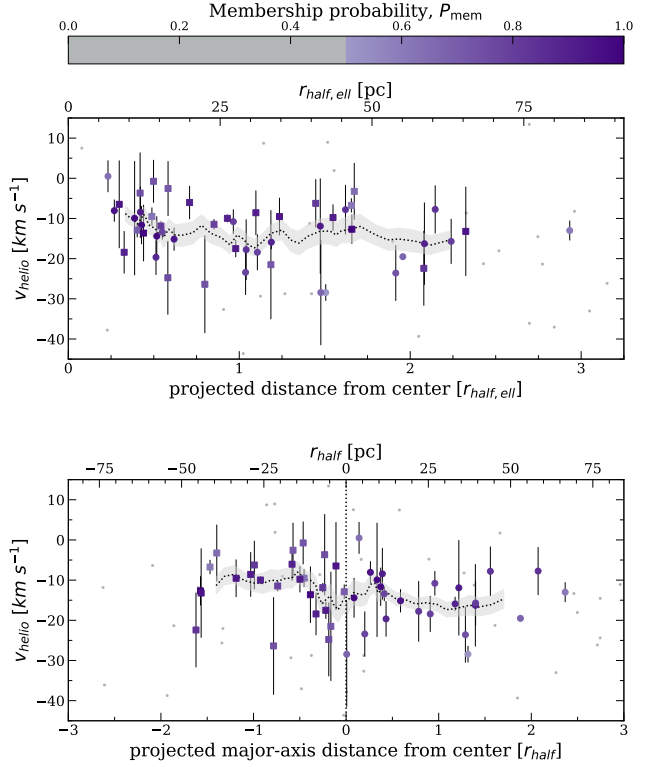


Figure 3: Heliocentric radial velocities and uncertainties of the 49 members as a function of elliptical half-light radius (*upper*) and projected distance with respect to the major axis (*lower*). For both plots, stars to the left and the right of the center axis of W1 are plotted as squares and circles, respectively. All 49 stars are color-coded purple according to their membership probability and non-members are in gray. In both panels, the dotted black line represents the membership probability weighted 7-star rolling velocity average, and the gray shaded region represents the uncertainty in the rolling average calculated via bootstrapping.

W1, although this is somewhat dependent on window size.

We find that this gradient is not obviously explained by ordered rotation (see Figure 3, lower panel).

We calculate the systemic velocity and velocity dispersion of W1 using a two-component Gaussian mixture model to simultaneously model the Milky Way and W1. We opt for this approach as it separates the two populations without imposing a strict membership threshold, allowing the inferred velocity dispersion to marginalize over contamination from Milky Way foreground stars (e.g., Martinez et al. 2011).

We begin by eliminating obvious non-members from our full dataset using the membership probabilities determined in §3.1. We define obvious non-members as stars whose membership probability without velocity ($P_{\text{mem,noy}} \propto P_{\text{CMD}} \times P_{\text{pm}} \times P_{\text{parallax}} \times P_{[\text{Fe}/\text{H}]}$) is less than 0.1 or stars with large radial velocities ($|v| > 150 \text{ km s}^{-1}$). This results in 65 stars within $3 r_{\text{half,ell}}$. Our results are not sensitive to our mem-

bership or velocity cut-off choices. We then apply a two-component Gaussian maximum likelihood function, whose total log likelihood takes the form (Walker et al. 2006):

$$\ln \mathcal{L} = \sum_i \ln [f \cdot \mathcal{N}(v_i | v_{W1}, \sigma_{W1}^2 + \delta v_i^2) + (1 - f) \cdot \mathcal{N}(v_i | v_{MW}, \sigma_{MW}^2 + \delta v_i^2)],$$

where f is the fraction of W1 members in our dataset, v_{W1} is the systemic velocity of W1, σ_{W1} is the velocity dispersion of W1, v_{MW} is the systemic velocity of the Milky Way, and σ_{MW} is the velocity dispersion of the Milky Way. We account for the velocity measurement uncertainty of each star, δv_i , by adding it in quadrature to the intrinsic dispersion of each Gaussian.

To sample this model, the MCMC sampler emcee (Foreman-Mackey et al. 2013) was run using 20 walkers. We initialize our walkers with the values from Willman et al. (2011) for W1 ($v_{W1} = -12.8 \text{ km s}^{-1}$, $\sigma_{W1} = 4.8 \text{ km s}^{-1}$, reasonable values for the Milky Way ($v_{MW} = 0 \text{ km s}^{-1}$, $\sigma_{MW} = 50 \text{ km s}^{-1}$), and a member fraction equivalent to the fraction of our determined member sample ($f = 0.75$), but our results are not dependent on these choices. We adopt the following uniform priors for our five parameters: $-100 < v_{MW} < 100 \text{ km s}^{-1}$, $0 < \sigma_{MW} < 200 \text{ km s}^{-1}$, $-30 < v_{W1} < 10 \text{ km s}^{-1}$, $0 < \sigma_{W1} < 10 \text{ km s}^{-1}$, $0 < f < 1$. The distribution of posterior samples is shown in the upper panel of Figure 4. We measure the systemic velocity as the sample median and the associated uncertainties from 16th and 84th percentiles.

The systemic velocity of W1 is estimated to be $v_{sys} = -13.0^{+1.1}_{-1.1} \text{ km s}^{-1}$ with a velocity dispersion of $\sigma_v = 4.7^{+1.5}_{-1.3} \text{ km s}^{-1}$, which is consistent with measurements by Willman et al. (2011). We highlight that the velocity dispersion is degenerate with the member fraction, implying that the large uncertainty in W1's velocity dispersion is driven by the uncertainty in identifying a pure member sample. This result is unchanged within the reported uncertainty when restricting the sample to anywhere within 2 to 4 $r_{\text{half,ell}}$, or when restricting the sample to only stars with multiple velocity epochs. When cutting the sample to 1 $r_{\text{half,ell}}$, the uncertainty on the velocity dispersion grows such that the system is not conclusively resolved due to the small sample size of stars. Notably, the kinematic distribution of W1 is asymmetric and non-Gaussian, suggesting that a single global velocity dispersion value is insufficient to fully characterize the complex kinematic profile of W1 (see Figure 4, bottom panel).

Assuming dynamical equilibrium, the dynamical mass of W1 within its half-light radius can be inferred from this radial velocity dispersion. Following the methods of Wolf et al. (2010), the mass of W1 within the half-light radius is estimated to be $\sim 5.9^{+3.8}_{-3.3} \times 10^5 M_\odot$, corresponding to a central mass-to-light ratio of $(M/L)_V = 660 \pm 600$. This is consistent with the dynamical mass and mass-to-light ratio previously

determined by Willman et al. (2011) ($\sim 3.9^{+2.5}_{-1.6} \times 10^5 M_\odot$; $(M/L)_V = 770^{+930}_{-440}$; note that we use an updated M_V value causing the mass-to-light ratio in this work to be smaller despite a larger mass).

The member fraction estimated from our mixture model is $f = 0.75^{+0.07}_{-0.08}$, which is consistent with the number of members determined in §3. We find similar results when employing a single Gaussian maximum likelihood model on our member sample of 49 stars within $3 r_{\text{half,ell}}$. From this method, the systemic velocity of W1 is measured to be $v_{sys} = -12.9^{+1.0}_{-1.0} \text{ km s}^{-1}$ with a velocity dispersion of $\sigma_v = 4.9^{+0.9}_{-0.8} \text{ km s}^{-1}$. Requiring multiple velocity epochs or reducing the half-light radius cut-off down to $2 r_{\text{half,ell}}$ does not alter the systemic velocity or velocity dispersion beyond the uncertainties determined. These results are consistent with the two-component Gaussian, but with likely underestimated uncertainties. As such, we emphasize our values from the mixture model which incorporate the uncertainty in membership as well. The properties of the 73 stars composing the 65 stars included in our mixture model and the 57 stars in our member sample are presented in Table A1.

4.2. Metallicity Distribution

As detailed in §2.2, we are able to infer [Fe/H] measurements for the stars in our member sample based on CaT equivalent width measurements. This calibration is only valid for RGB stars ($M_V < 3$), significantly reducing our member sample to 8 stars with measured metallicities (see Figure 2, lower panel; Figure 5, upper panel). From this sample, we determine the CaT-based mean metallicity and metallicity dispersion using an MCMC sampler with 20 walkers to sample from a Gaussian maximum likelihood function (Foreman-Mackey et al. 2013; Walker et al. 2006). We opt not to use a mixture model as performed in §4.1 due to the small sample size and lack of borderline stars with measured metallicities (see Figure 1h). We initialize our walkers using the values determined by Willman et al. (2011) ($[\text{Fe}/\text{H}] = -2.1$, $\sigma_{[\text{Fe}/\text{H}]} = 0.45 \text{ dex}$). The median and 16th and 84th percentiles of the resulting posterior distribution function are presented.

The metallicity of W1 is measured to be $[\text{Fe}/\text{H}] = -2.45^{+0.13}_{-0.13}$ with a metallicity dispersion of $\sigma_{[\text{Fe}/\text{H}]} = 0.30^{+0.15}_{-0.11} \text{ dex}$ (see Figure 5). The removal of the highest metallicity star slightly lowers the measured average metallicity and substantially reduces the measured metallicity spread (to $[\text{Fe}/\text{H}] = -2.54^{+0.09}_{-0.09}$, $\sigma_{[\text{Fe}/\text{H}]} = 0.12^{+0.12}_{-0.08} \text{ dex}$). We emphasize that this star has a high membership probability ($P_{\text{mem}} \sim 0.9$) and that the mean metallicity without this star is still within the uncertainties derived with the full sample.

Willman et al. (2011) measured a metallicity spread in W1 based on Keck/DEIMOS spectroscopy of three RGB members ($[\text{Fe}/\text{H}] = -1.73 \pm 0.12$, -2.65 ± 0.12 , and -1.92 ± 0.21). These three stars are in our member sample, although we re-

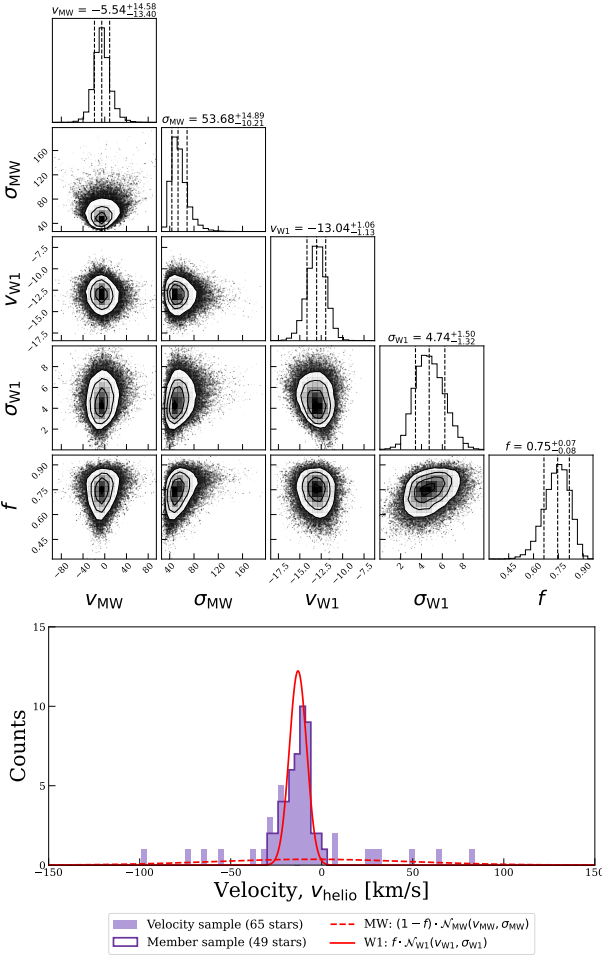


Figure 4: *Upper*: Posterior samples for the two-component Gaussian mixture model to measure the systemic velocity and velocity dispersion of W1 based on a velocity sample of 66 potential member stars within $3 r_{\text{half,ell}}$. The dashed lines represent the median value and 16th and 84th percentiles. *Lower*: Best-fit mixture model of two-component Gaussian representing the Milky Way and W1. The 65 potential members used for our fitting are over-plotted, and the member sample (§3.2) is outlined in purple. We note the asymmetric velocity distribution and comment on this in §7.2.

port slightly lower metallicity values for two of these stars ([Fe/H] = -2.31 ± 0.13 , -2.56 ± 0.13 , and -2.60 ± 0.19 , respectively). In comparison with the photometric metallicity values derived from *HST* CaHK imaging from Fu et al. (2023), we measure W1 to be a slightly more metal-rich system with a substantially smaller metallicity dispersion than their values of ([Fe/H] = $-2.53^{+0.11}_{-0.11}$, $\sigma_{\text{[Fe/H]}} = 0.65^{+0.10}_{-0.09}$ dex).

5. MASS SEGREGATION

We now shift our attention to the *HST*/ACS data (§5.1), evaluating the presence of stellar mass segregation which can be used to differentiate between a galactic and star cluster origin for W1 (§5.2).

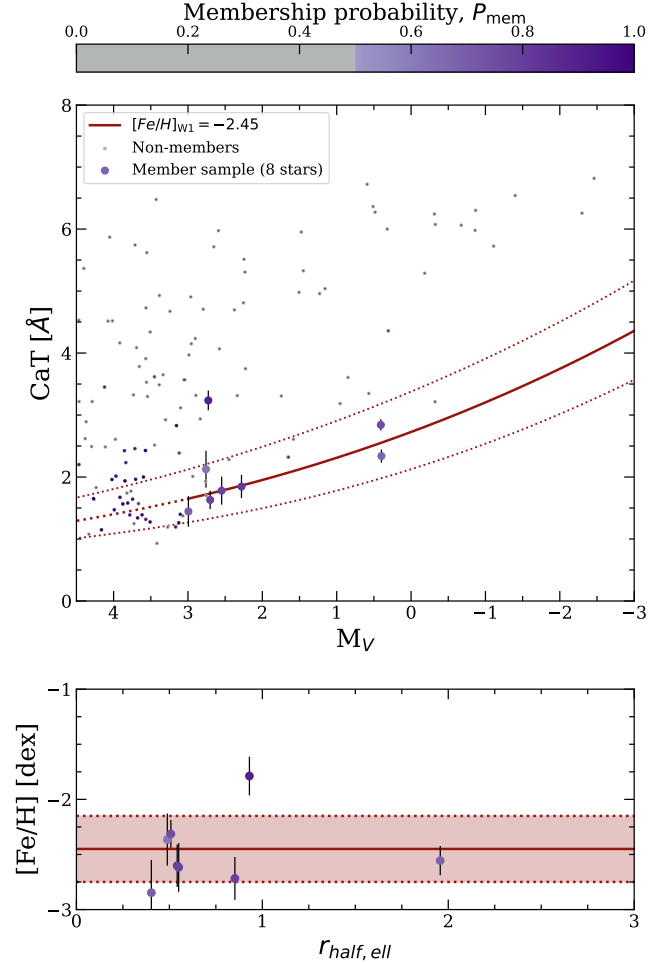


Figure 5: CaT equivalent width as a function of V-band magnitude (*upper*) and the CaT-based spatial metallicity distribution (*lower*) for the 6 RGB stars in our member sample. The solid line denotes the calibration range of the empirical relationship of Carrera et al. (2013) plotted at the mean metallicity of W1 while the dotted lines represents the metallicity dispersion determined from MCMC sampling.

5.1. *HST*/ACS Imaging

W1 was observed by the *Hubble Space Telescope* (*HST*) in 2017 as part of the Treasury Program GO-14734 (PI-Kallivayalil). Deep photometry of W1 was obtained with the Advanced Camera for Surveys (ACS; Ford et al. 1998) using the Wide Field Channel (WFC). The ACS/WFC field approximately covers the inner half-light radius of W1 (see Figure 2, upper panel). Observations were split evenly between the F606W and F814W filters with a combined exposure time of 9254 seconds.

For the analysis below, we use the same *HST* data reduction as described in Richstein et al. (2024). Briefly, the individual exposures from each filter were aligned and co-added

using DrizzlePac, an *HST* software package. The combined output images were then masked with the `segmentation` routine from the `photutils` package (Bradley et al. 2025). PSF-fitting photometry was performed on the combined images using DAOPHOT-II and ALLSTAR (Stetson 1987, 1992). The source lists from F606W and F814W were matched using DAOMATCH and DAOMASTER to create a preliminary PSF source catalog. An empirically-derived aperture correction was applied to the magnitudes, which were then converted to the VegaMag system and adjusted for the exposure time. Finally, to address star-galaxy separation, each source was assigned a quality flag from 0 to 1 based on how closely its parameters matched those in artificial star tests across different filters.

We also note that Durbin et al. (2025) used *HST* imaging to measure the star formation histories of 36 ultra-faint dwarf galaxies, including W1. Their results indicate that 50% of W1's stellar mass formed $\tau_{50} = 13.44^{+0.00}_{-0.81}$ Gyr and 90% of W1's stellar mass formed before $\tau_{90} = 8.37^{+0.08}_{-0.93}$ Gyr, indicating a uniformly ancient stellar population formed from an early burst of star formation. We obtain consistent results when performing the same star formation history analysis on this dataset ourselves.

5.2. Mass Segregation Determination

The presence of mass segregation can be used as a diagnostic for determining whether a system is a star cluster or a dwarf galaxy (Baumgardt et al. 2022). Due to the equipartition of kinetic energy whereby high-mass stars transfer energy to low-mass stars over time, high-mass stars tend to aggregate near the center of systems while low-mass stars drift towards the outer regions. This process occurs over the course of a few relaxation periods, and is thus a significant feature in old stellar objects with relatively short relaxation periods compared to their age, such as globular clusters (e.g., Tripathi et al. 2023; Kim et al. 2015; Weatherford et al. 2020). For systems with substantial amounts of dark matter such as ultra-faint dwarf galaxies, the system's relaxation period is prolonged beyond a Hubble time such that mass segregation is unobservable (Longeard et al. 2018).

Baumgardt et al. (2022) first evaluated the presence of mass segregation in W1 using *HST/ACS* imaging by comparing the cumulative radial distribution of stars in the upper and lower regions of the main sequence (MS), effectively creating two samples: one of bright, higher-mass stars and the other of faint, lower-mass stars. While the ratio of half-light radii for these two samples usually lies around 0.7 for highly segregated systems such as old globular clusters, Baumgardt et al. (2022) measured a ratio of $R_{\text{half,bright}}/R_{\text{half,faint}} = 1.05 \pm 0.08$ for W1, indicating a lack of mass segregation and evidence towards a dwarf galaxy classification.

Loosely following the methods of Baumgardt et al. (2022), we re-analyze the same *HST/ACS* data to rigorously evaluate the possibility of mass segregation in W1. First, we re-

move extragalactic sources, defined as those with star quality flags > 0.7 . To isolate the probable member stars in W1, we compared the CMD of the 1,055 remaining stars to an old, metal-poor isochrone from the MIST stellar evolutionary track models ($\tau = 12$ Gyr, $[\text{Fe}/\text{H}] = -2$, shifted to a distance modulus of $m - M = 17.93$ which corresponds to a distance of 38.55 kpc), accounting for interstellar reddening (Dotter 2016; Choi et al. 2016; Sirianni et al. 2005; Schlegel et al. 1998). We define members as stars with the greater of either 0.15 mag or twice their photometric uncertainty from the isochrone. Finally, due to the limited field of view of the ACS/WFC compared to the extended spatial distribution of W1, only stars contained within $1 r_{\text{half,ell}}$ were included to ensure that the mass segregation profile was not controlled by just a few outlying stars. Our final sample consists of 635 stars.

We use the MS turnoff and the estimated location of $0.5M_{\odot}$ stars included in the synthetic isochrone as upper and lower photometric bounds. The stars that passed the spatial and CMD cuts within these bounds were divided into two groups of equal size based on stellar brightness to create two separate samples of bright and faint stars (see Figure 6). The radial cumulative distribution of stars for each sample was determined using an elliptical aperture with half-light radius, position angle, and ellipticity values from Martin et al. (2008) (see Table 2). Additionally, the half-light radius for each sample was defined as the elliptical radius within which half of the stars of each sample are contained.

Baumgardt et al. (2022) estimated that the expected half-light ratio between bright and faint stars for a star cluster the size of W1 is 0.90, a value which would only be more extreme if W1 is tidally disturbed as both mass segregation and tidal stripping would preferentially remove low-mass stars from the central regions (Paust et al. 2009). We obtained a half-light radius ratio of $R_{\text{half,bright}}/R_{\text{half,faint}} = 1.05 \pm 0.09$, where the uncertainty is calculated by bootstrapping over each sample. A standard two-sample KS test shows a $<1\%$ probability of mass segregation, which we highlight as a more comprehensive test statistic that takes into account the full distributions rather than evaluating the discrepancy between distributions at a single location (see Figure 6). This process was repeated using varying lower bound cut-offs all the way down to the 50% photometric completeness limit. Most of the results of these varied samples are consistent with an unsegregated system, with only a few samples showing inconclusive results (that is, with values compatible with both a segregated and unsegregated system). We emphasize that a few inconclusive results should not be over-interpreted due to potential unresolved galaxy contamination at fainter magnitudes and a limited sample size at brighter magnitudes that could produce false positive results from large uncertainties. We also tested for mass segregation using a circular aperture, which gave slightly higher half-light radius ratios, more consistent with the results of Baumgardt et al. (2022) who

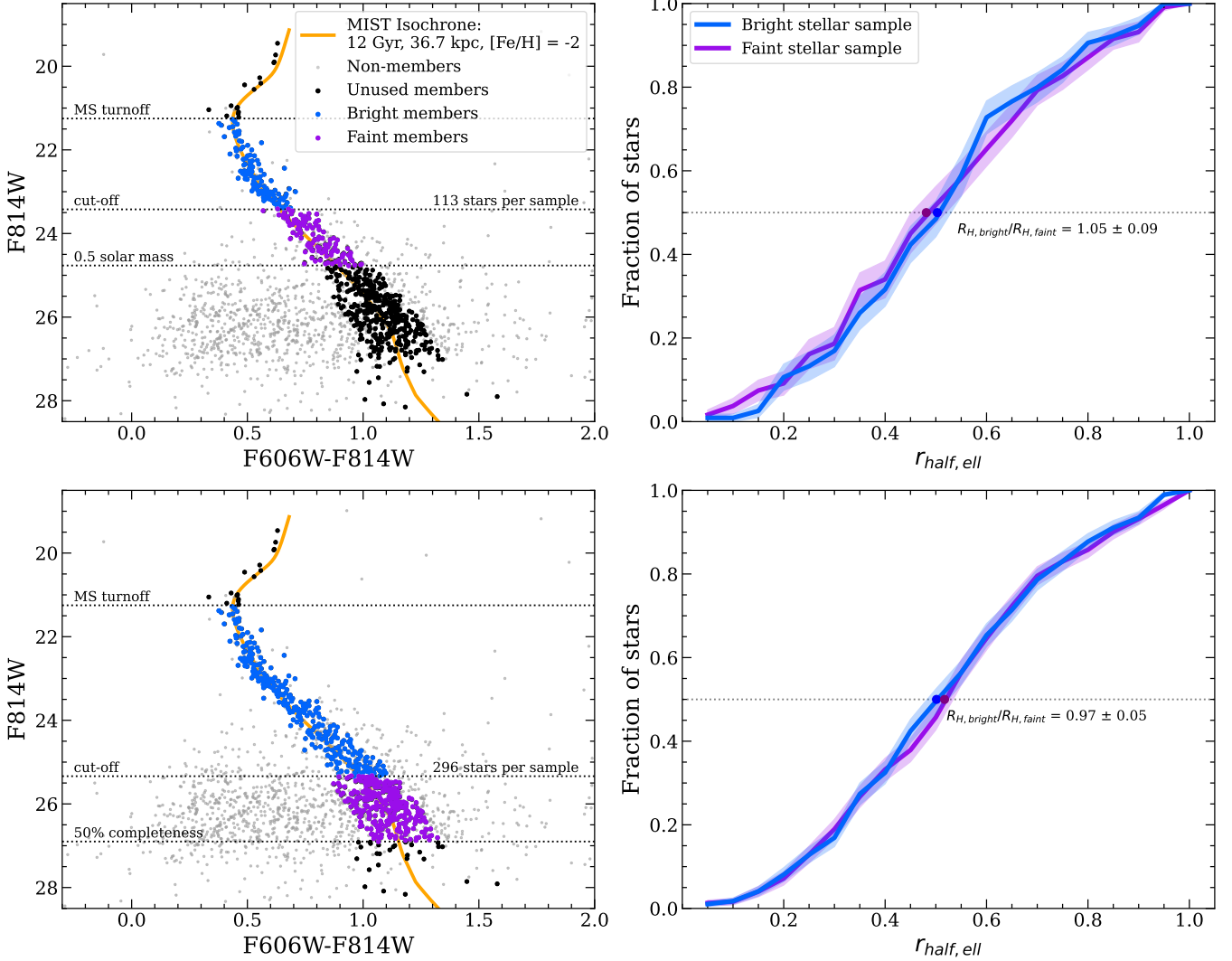


Figure 6: Mass segregation analysis of W1 from *HST/ACS* observations. *Left:* CMD of W1 *HST* data overlaid with an old, metal-poor MIST isochrone in orange. Blue and purple stars show the stars selected based on different magnitude cuts (*upper* = $0.5M_{\odot}$; *lower* = 50% completeness threshold) to calculate the mass segregation profile. *Right:* Corresponding average cumulative elliptical radial distribution of stars. The shaded region corresponds to the 1- σ uncertainty calculated by bootstrapping over each sample. No significant signs of mass segregation are detected.

also used a circular aperture. All KS tests performed had probabilities of mass segregation less than 29.7%, the value determined by Baumgardt et al. (2022).

It should be noted that the follow-up paper to the discovery of W1 presented evidence for mass segregation when comparing the luminosity function (LF) of stars in the central and tail regions (Willman et al. 2006, Fig. 4). Observing an excess of low luminosity stars in the tail region, they performed a KS test that showed a 68% chance that the two stellar LFs were drawn from different populations, which was interpreted as evidence for mass segregation. To revisit this claim using a larger sample size and deeper photometry, the 635 *HST* member stars were divided into two samples by implementing similar cuts to Willman et al. (2006): central stars

within $0.5r_{\text{half,ell}}$ and outer stars beyond $0.5r_{\text{half,ell}}$. As carried out by Willman et al. (2006), the LF for each sample was determined and an offset value was added to the central region sample to correct for a difference in sample size and facilitate direct comparison. No surplus of low luminosity stars are observed in the outer stars and performing a two-sample KS test on the inner and outer sample LFs shows a < 10% probability that the two LFs were drawn from different populations, which we interpret as additional evidence that W1 is unsegregated. As one final check, this process was repeated for 57 member stars from our analysis of the DEIMOS data (§3.2), which also show no excess of low luminosity stars at the outskirts. Thus, consistent with the results of Baumgardt et al. (2022), our analysis does not find evidence for mass

654 segregation in W1, supporting a dwarf galaxy classification
 655 for W1.

656 6. DYNAMICAL HISTORY

657 We next investigate the possibility of past tidal interactions
 658 between the Milky Way and W1 by examining the orbital his-
 659 tory of W1 (§6.1) and simulating mock stellar streams (§7.2).

660 6.1. Orbital solutions

661 To model the orbit of W1, we use an analytic potential,
 662 which has been shown to be generally accurate for low-mass
 663 satellites that have not been severely disrupted (Machado
 664 et al. 2025). Previous orbital analyses of Milky Way dwarf
 665 galaxies have reported moderately small pericenter values for
 666 W1 (ranging from 16 kpc to 44 kpc; Pace et al. 2022; Simon
 667 2018; Armstrong et al. 2021), but are highly dependent on
 668 membership selection and the assumed Milky Way potential.

669 Using the `galpy` package by Bovy (2015), we integrate the
 670 orbit of W1 backwards in time based on its 6D phase-space
 671 coordinates (see Table 2 for values). We measure a proper
 672 motion of $(\mu_a^*, \mu_\delta) = (0.303 \pm 0.052, -1.094 \pm 0.075)$ mas
 673 yr⁻¹ by using a single Gaussian maximum likelihood model
 674 on the 7 stars in our member sample with measured *Gaia*
 675 proper motions (see Figure 1g). This is consistent with the
 676 results of Pace et al. (2022), who apply background mixture
 677 models to *Gaia* EDR3 data, both in measurement value and
 678 the number of *Gaia* members.

679 To model the Milky Way’s gravitational potential, we
 680 adopted `MWPotential2014` of Bovy (2015), which consists
 681 of a power-law spherical potential represents the bulge (Bin-
 682 ney & Tremaine 1987), a Miyamoto-Nagai disk potential
 683 (Miyamoto & Nagai 1975), and a NFW dark matter halo
 684 potential (Navarro et al. 1997). The estimate of the mass
 685 of the Milky Way’s dark matter halo for `MWPotential2014`
 686 is on the lower end with a value of $0.8 \times 10^{12} M_\odot$. To ac-
 687 count for this uncertainty, we also model W1’s orbit using
 688 the same potential but with a 50% larger dark matter halo
 689 mass ($1.2 \times 10^{12} M_\odot$). The Large Magellanic Cloud (LMC)
 690 has also been known to affect the orbits of objects, even those
 691 distant from it, due to the reflex-motion of the Milky Way’s
 692 orbit (e.g., Erkal et al. 2021; Ji et al. 2021; Correa Magnus &
 693 Vasiliev 2022; Patel et al. 2024). This MW+LMC potential
 694 is the third and final potential we use to calculate the orbit
 695 of W1, where the LMC is modeled by a moving Hernquist
 696 potential of mass $1.38 \times 10^{11} M_\odot$ and scale radius of 8.7 kpc,
 697 taking into account dynamical friction (Bovy 2015; van der
 698 Marel & Kallivayalil 2014; Hernquist 1990). We find the
 699 dynamical friction of W1 to have a negligible impact on its
 700 orbit. Due to uncertainty in orbit integration models beyond
 701 one orbital period (especially for satellites with a pericenter
 702 < 30 kpc, D’Souza & Bell 2022; Machado et al. 2025), we
 703 use these potentials to model the 3-dimensional orbit of W1
 704 over only the last 1 Gyr with a time resolution of 1 Myr.

705 Figure 7 compares the modeled orbits of W1 using these

706 three different Milky Way potentials. The orbital period pre-
 707 dicted by the original `MWPotential2014` is larger than the
 708 other two potentials by ~ 0.2 Gyr. In all cases, W1 is pre-
 709 dicted to be coming from a position closer to the galactic
 710 center, although the exact pericenter of the orbit depends on
 711 the potential used.

712 Due to the uncertainties in distance, velocity, and proper
 713 motion measurements, the uncertainty in the orbit of W1
 714 was calculated through Monte Carlo sampling. 1,000 six-
 715 dimensional phase-space coordinates were created by sam-
 716 pling distance, velocity, and proper motion values from
 717 Gaussian distributions based on each parameter’s average es-
 718 timated value and 1- σ standard deviation (see Table 2). The
 719 reported distance uncertainty from Durbin et al. (2025) is
 720 likely underestimated as it does not include systematic con-
 721 tributions from the isochrones. Our orbital solutions remain
 722 conclusively consistent with a system moving away from a
 723 position closer in to the Milky Way up to distance uncertain-
 724 ties of ~ 3 kpc.

725 This procedure was performed for both the regular
 726 `MWPotential2014` and the potential with the addition of the
 727 LMC, as shown in Figure 7. The orbit of W1 under the reg-
 728 ular `MWPotential2014` has a pericenter of $r_{\text{peri}} = 24.9^{+3.5}_{-2.9}$
 729 kpc, an apocenter of $r_{\text{apo}} = 43.4^{+0.5}_{-0.5}$ kpc, and an eccentric-
 730 ity $e = 0.27^{+0.06}_{-0.06}$ while the the addition of the LMC alters
 731 these predictions, simulating a pericenter of $r_{\text{peri}} = 14.8^{+1.9}_{-1.6}$
 732 kpc, an apocenter of $r_{\text{apo}} = 43.2^{+0.5}_{-0.5}$ kpc, and an eccentric-
 733 ity of $e = 0.49^{+0.04}_{-0.05}$. These reported parameters represent
 734 the median of our sampling procedure, and the uncertainties
 735 represent the 14th and 86th percentiles. None of the orbital
 736 samples for both potentials have pericenters greater than 40
 737 kpc, indicating that the trajectory of W1 is most likely to be
 738 coming out of the Milky Way and approaching the apocenter
 739 of its orbit.

To quantitatively verify that W1 is at the apocenter of its
 orbit, we calculated the ratio f_{peri} of Fritz et al. (2018):

$$740 f_{\text{peri}} = \frac{r_{\text{GC}} - r_{\text{peri}}}{r_{\text{apo}} - r_{\text{peri}}}, \quad (6)$$

741 which is a proxy for the orbital phase in the radial direc-
 742 tion. $f_{\text{peri}} = 0$ and 1 indicate an object at the pericenter
 743 and apocenter of its orbit, respectively. For both the regu-
 744 lar `MWPotential2014` and with the addition of the LMC,
 745 the ratio was determined to be $f_{\text{peri}} = 0.99 \pm 0.01$, consis-
 746 tent with our conclusion that W1 is being observed at or very
 747 near the apocenter of its orbit after spending time closer to
 the galactic center.

748 From the estimate of the central dynamical mass of W1
 (M_{W1}), the Jacobi tidal radius of W1 (R_J) as a function of
 orbital radius (R_{W1}) can be approximated (Innanen et al.
 1983):

$$749 R_J(R) = \left(\frac{M_{\text{W1}}}{3M_{\text{MW}}^*} \right)^{1/3} R_{\text{W1}} \quad (7)$$

750 The mass of the Milky Way enclosed within the or-

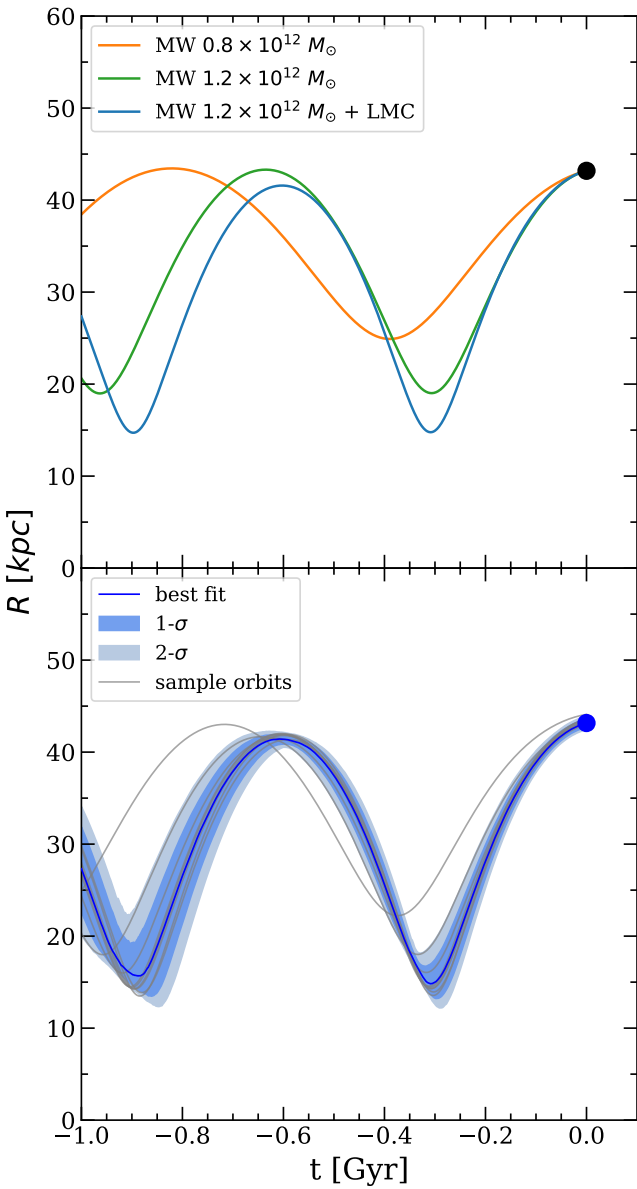


Figure 7: Orbit of W1. *Upper:* Distance of W1 to the galactic center as a function of time using three different Milky Way potentials from [Bovy \(2015\)](#) orbital simulations. *Lower:* Same as above but only showing the orbital simulations using `MWPotential2014` of [Bovy \(2015\)](#), with the dark matter halo mass scaled up by 50% and the addition of the LMC. The blue line represents the 50th percentile orbit from Monte Carlo sampling over the 6D phase space parameter uncertainties, the dark blue shaded region represents the space within the 16th and 84th percentile orbits, and the light blue region represents the space between the 5th and 95th percentile orbits.

⁷⁴⁹ bital radius of the satellite (M_{MW}^*) was determined from
⁷⁵⁰ `MWPotential2014` with a dark matter halo mass enlarged
⁷⁵¹ by 50% ($1.2 \times 10^{12} M_{\odot}$). From this, the current Jacobi tidal

⁷⁵² radius of W1 is estimated to be $R_J = 220^{+120}_{-140}$ pc, which cor-
⁷⁵³ responds to $7.7^{+1.6}_{-1.8}$ half-light radii. In comparison, the tidal
⁷⁵⁴ radius of W1 at the pericenter of its orbit is $R_J = 88^{+51}_{-57}$ pc,
⁷⁵⁵ which is equivalent to $3.1^{+0.8}_{-0.8}$ half-light radii. These simula-
⁷⁵⁶ tions suggest that, at its pericenter, the Jacobi radius of W1
⁷⁵⁷ was within a few half-light radii of its center.

⁷⁵⁸ The current dynamical properties of a satellite also corre-
⁷⁵⁹ spond to their infall time, as shown by [Rocha et al. \(2012\)](#)
⁷⁶⁰ using subhalos from the Via Lactea II cosmological simu-
⁷⁶¹ lations. Their work found a tight correlation between orbital
⁷⁶² energy and infall time where subhalos that were accreted ear-
⁷⁶³ lier had more time to sink into the gravitational potential of
⁷⁶⁴ the Milky Way, resulting in energies corresponding to more
⁷⁶⁵ tightly bound systems (see Fig. 2 of [Rocha et al. 2012](#)).
⁷⁶⁶ Tightly bound objects cluster at small Galactocentric radii
⁷⁶⁷ and low speeds (see Fig. 3 [Rocha et al. 2012](#)), consistent
⁷⁶⁸ with the properties of W1 (see Figure 10, center panel). In-
⁷⁶⁹ deed, our orbital model for W1 suggests that W1 is one of
⁷⁷⁰ the most tightly bound dwarf galaxies based on its total en-
⁷⁷¹ ergy. From this relation, we estimate W1’s infall time to be
⁷⁷² roughly 9 Gyr ago. Combining this with an orbital period of
⁷⁷³ ~ 0.6 Gyr (see Figure 7, bottom panel), we can estimate that
⁷⁷⁴ W1 has undergone ~ 15 orbits since it crossed into the virial
⁷⁷⁵ radius of the Milky Way.

6.2. Mock tidal streams

⁷⁷⁶ To further probe the possibility of tidal interactions be-
⁷⁷⁷ tween the Milky Way and W1, we used the `gala` parti-
⁷⁷⁸ cle stream spray to generate simulated stellar streams to
⁷⁷⁹ compare with the distribution of W1 stars. The same six-
⁷⁸⁰ dimensional phase-space coordinates and Milky Way gravi-
⁷⁸¹ tational potential as used in the orbit integration was adopted
⁷⁸² ([BovyMWPotential2014](#), 50% enlarged dark matter halo).
⁷⁸³ The mass of the simulated progenitor object was set to
⁷⁸⁴ $5.8 \times 10^5 M_{\odot}$ (the central dynamical mass of W1 determined
⁷⁸⁵ in §4.1) and a scale radius of 26.8 pc (the approximate half-
⁷⁸⁶ light radius of W1) was used to represent W1. From this,
⁷⁸⁷ the self-gravity of W1 was modeled by a Plummer potential
⁷⁸⁸ ([Willman et al. 2011; Plummer 1911](#)). The orbit of W1 was
⁷⁸⁹ integrated backwards in time over 1 Gyr in 1 Myr intervals,
⁷⁹⁰ and then re-integrated forward in time to the present such that
⁷⁹¹ a particle was sprayed at each of the two Lagrange points at
⁷⁹² each time step following the Fardal Stream distribution func-
⁷⁹³ tion ([Fardal et al. 2015](#)).

⁷⁹⁴ The results of these simulations, as summarized by Figure
⁷⁹⁵ 8, show that the average solar-reflex-corrected proper mo-
⁷⁹⁶ tion vector seems to roughly align with the orbital trajectory.
⁷⁹⁷ The spatial spread of the mock streams is quite large with the
⁷⁹⁸ highest areas of density approximately along the semi-major
⁷⁹⁹ axis of W1.

7. DISCUSSION

7.1. Is W1 a dwarf galaxy?

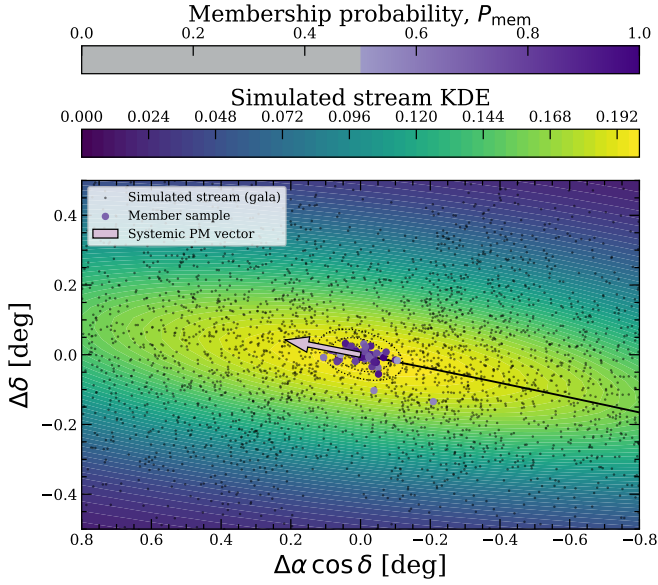


Figure 8: Spatial distribution of simulated data from gala mock stream spray model using `MWPotential2014` of [Bovy \(2015\)](#) with a 50% enlarged dark matter halo ($1.2 \times 10^{12} M_{\odot}$). The member sample is over-plotted and color-coded according to their membership probability. The systemic proper motion vector corrected for solar reflex motion is denoted by the light purple arrow, and the three concentric dotted ellipses represent the space within 1, 2, and 3 $r_{\text{half,ell}}$.

We now turn to the question of the nature of W1: is this object a dwarf galaxy or a star cluster? From our kinematic analysis (§4.1), we measure a mass-to-light ratio of 660 ± 600 from the 49 non-variable member stars within $3 r_{\text{half,ell}}$. This large mass-to-light ratio that is far from unity is indicative of a dark matter-dominated object (e.g., [Martin et al. 2007; Simon & Geha 2007](#)). We emphasize that cutting to within different half-light radii down to $2 r_{\text{half,ell}}$ does not change our results. From our metallicity analysis (§4.2), we find evidence for a metallicity spread ($\sigma_{[\text{Fe}/\text{H}]} = 0.30^{+0.15}_{-0.11}$ dex) based on 6 RGB stars with measured spectroscopic metallicities. This metallicity spread suggests that W1 has undergone chemical enrichment, a property of satellites with dark matter halos that allow them to retain their gas more efficiently and go through successive epochs of star formation (e.g., [Willman & Strader 2012; Kirby et al. 2013b](#)).

We conduct a comprehensive search for the presence of mass segregation in W1 based on *HST/ACS* imaging (§5). We find a lack of mass segregation, implying a dwarf galaxy classification and consistent with previous work of [Baumgardt et al. \(2022\)](#). While recent simulations by [Errani et al. \(2025\)](#) suggest that mass segregation can occur in very low stellar mass objects, even if they host a dark matter halo. However, this does not apply to W1 who has a large size and luminosity compared to the objects studied, which prolongs its relaxation time beyond a Hubble time.

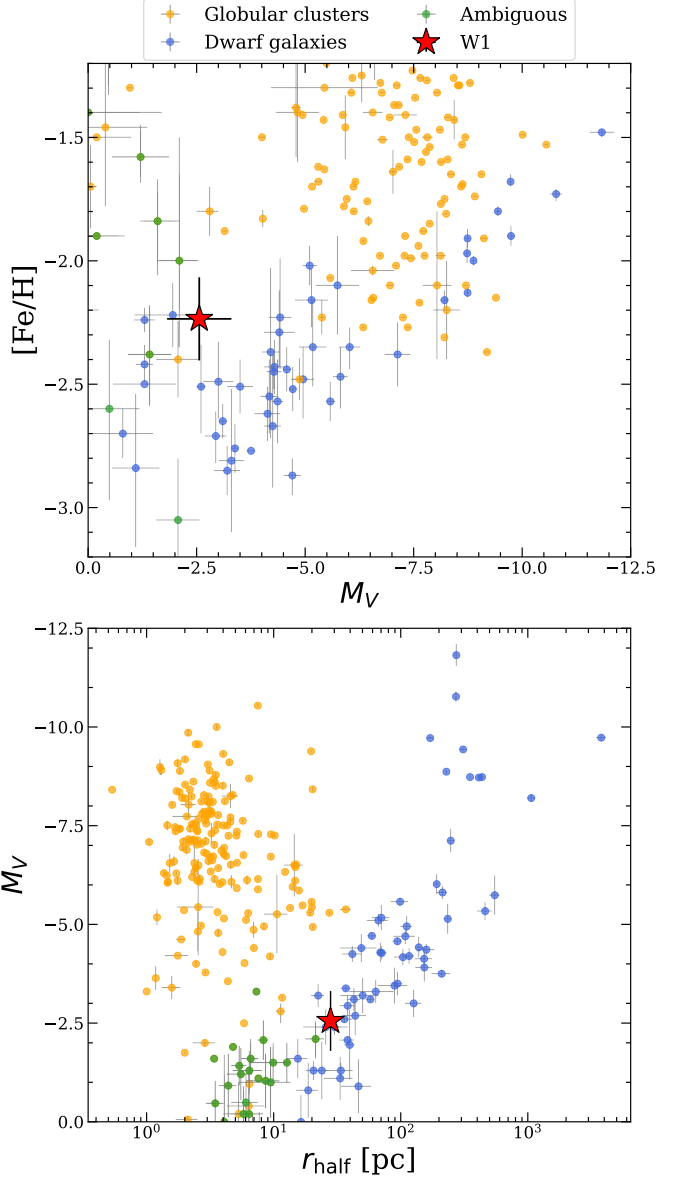


Figure 9: Comparison of W1 (red star) with other Milky Way dwarf galaxies (blue circles), globular clusters (orange circles), and ambiguous objects (green circles) taken from ([Pace 2025](#)). *Upper:* [Fe/H] iron abundance spectroscopic metallicity as a function of absolute V-band magnitude. W1 is significantly fainter compared to other dwarf galaxies in its metallicity range, which could be explained by mass loss due to tidal stripping. *Lower:* Absolute V-band magnitude as a function of half-light radius. W1 is one of the faintest dwarf galaxies and has one of the smallest half-light radii.

Finally, we compare the structural properties of W1 to other Milky Way satellites. We rely on the Local Volume Database of [Pace \(2025\)](#) for a comprehensive repository of the latest literature values of the observed properties of Milky Way dwarf galaxies, globular clusters, and ambiguous objects. The position of W1 on the size-luminosity plane of

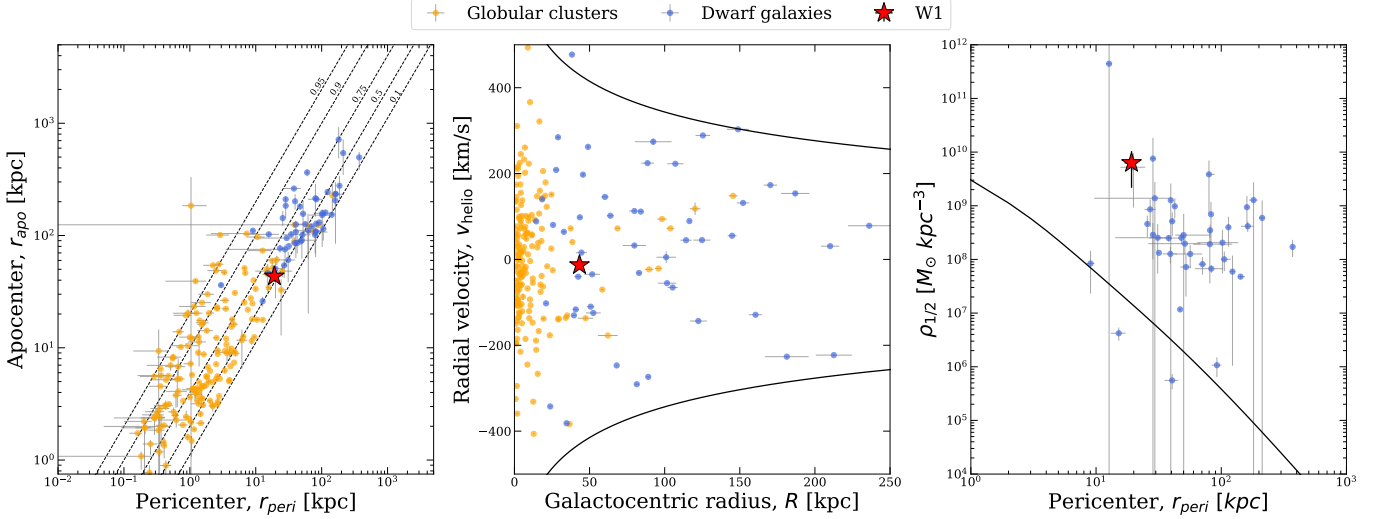


Figure 10: Comparison of the orbital properties of W1 with other Milky Way dwarf galaxies and globular clusters. W1 is denoted by a red star (see Table 2), Milky Way dwarf galaxies as blue circles, and globular clusters as orange circles (Pace 2025). *Left:* Apocenter as a function of pericenter. The locations of different orbital eccentricities are labeled as dotted lines. W1 has a small pericenter and apocenter relative to other Milky Way dwarf galaxies. *Center:* Radial velocity as a function of Galactocentric radius, which corresponds to its binding energy and infall time (Rocha et al. 2012). The black lines represent the curves for bound systems for MWPotential2014 of Bovy (2015) with a 50% enlarged dark matter halo. W1 has one of the smallest radial speeds and Galactocentric radii, corresponding to a high binding energy and early infall time (see §6.1). *Right:* Average density within one half-light radius as a function of orbital pericenter. The black line shows twice the enclosed Milky Way density as a function of radius. According to Pace et al. (2022), if the satellite sits below this line, its Jacobi radius will be larger than the half-light radius and it will likely be tidal disrupting.

confirmed Milky Way satellites suggests that its classification is more consistent with the population of dwarf galaxies; W1 is significantly less compact than globular clusters with similar luminosities (see Figure 9; upper panel).

Overall, due to its large mass-to-light ratio, observed metallicity spread, lack of mass segregation, and position on the size-luminosity plane, we conclude that W1 is a dwarf galaxy.

7.2. Is W1 tidally disrupted?

The total mass of satellite systems are estimated under the assumption of dynamical equilibrium (Wolf et al. 2010). It is thus crucial to understand the dynamical state of W1 in order to determine whether its measured internal velocity dispersion is a true reflection of its dynamical mass. We will now weigh the evidence for and against tidal disruption.

The evidence for tidal disruption is the following. First, the spatial distribution of W1 is elongated, with an ellipticity of $\epsilon = 0.47$ (Muñoz et al. 2018b). Crucially, the stars with high membership probabilities are not confined to the central regions, but also include stars near the outskirts. Although we do not see the presence of extended spatial features beyond $4 r_{half,ell}$ as suggested by previous work and we report that the number density of stars is consistent with the expected Plummer distribution, this is not inconsistent with simulations of mildly stripped satellites (e.g., Peñarrubia et al. 2009).

Second, we continue to observe an irregular velocity pro-

file, as originally noted in Willman et al. (2011), where the velocities of stars within $\sim 0.75 r_{half,ell}$ are systematically higher (see Figure 3, upper panel). This also results in a remarkably asymmetric, non-Gaussian velocity profile (see Figure 4, lower panel). Furthermore, we find that the velocity dispersion of the central member stars within $1 r_{half,ell}$ is significantly lower than the velocity dispersion measured out to $2 - 4 r_{half,ell}$, even when accounting for Milky Way interlopers via Gaussian mixture modeling.

The luminosity-metallicity relation has been shown to be tight for dwarf galaxies (Kirby et al. 2013b; Simon 2019). For satellites that initially conform to this relation, tidal stripping decreases their luminosity while the average metallicity is unchanged; this property has been used as a diagnostic for tidal stripping (e.g., Kirby et al. 2013a, 2015; Collins et al. 2020). We find evidence for this phenomenon in the case of W1 where the luminosity of W1 is much fainter when compared to dwarf galaxies of similar metallicities (see Figure 9, upper panel).

Our simulations of tidal streams for a W1-like progenitor show that W1's elongated structure is along the same axis as the highest areas of density of the mock streams. These features are also aligned with the orbital trajectory of W1, consistent with the hypothesis that tidal stripping from the Milky Way's gravitational field could explain W1's elongated and elliptical spatial distribution.

We also compare the orbital parameters of W1 with those of other Milky Way dwarf galaxies and globular clusters in Figure 10. These parameters were determined by assuming the MWPotential2014 with dark matter halo mass enlarged by 50% and with the addition of the LMC. We Monte Carlo sample over the 6D phase space parameter uncertainties, the same methods as performed on W1 (§6.1). Our best-fit orbital solutions for W1 conclusively predict W1 to currently be at the apocenter of its orbit, coming from a position closer to the galactic center. Our models show evidence for a pericentric passage $\lesssim 25$ kpc, where the Jacobi radius of W1 would be on the order of a few half-light radii, potentially allowing for the stripping of stars at the outskirts. Compared to other Milky Way dwarf galaxies, W1 is moderately elongated and both its pericenter and apocenter are relatively small (see Figure 10, left panel). From W1’s orbital properties, we predict an infall time of roughly 9 Gyr. W1 has one of the smallest radial speeds and Galactocentric radii of the Milky Way’s dwarf galaxies, consistent with a system with a high binding energy and early infall time (see Figure 10, center panel). This infall time corresponds to roughly 15 orbits completed since W1 crossed into the virial radius of the Milky Way. In combination with the small pericenter and apocenter of W1, this suggests that slow tidal stripping from W1’s sustained passage near the Milky Way over the course of its orbit could explain W1’s elongated structural properties and irregular kinematic profile.

The evidence against tidal disruption is W1’s large density, which implies that its half-light radius is smaller than its Jacobi radius (see Figure 10, right panel). However, we note multiple other dwarf galaxies with evidence for tidal disruption also lie above this line (e.g., Boötes I, Hercules, Filion & Wyse 2021; Ou et al. 2024). If W1 is indeed tidally disrupted and exhibits a large density, this could suggest that tidal stripping is more efficient than previously thought.

8. CONCLUSION

We have presented a comprehensive study of the structural, kinematic, chemical, and orbital properties of W1. Our main conclusions are summarized as follows:

- We apply a probabilistic membership approach that factors in a star’s position on the CMD, radial velocity, metallicity, and *Gaia* proper motion and parallax measurements when available to new and improved Keck/DEIMOS spectroscopy (§2, 3.1). From this, we identify a member sample of 57 stars, including 6 binaries (§3.1). We measure physical properties from 49 of these stars out to 3 half-light radii.
- We measure a systemic velocity of $v_{\text{sys}} = -13.0^{+1.1}_{-1.1}$ km s $^{-1}$ and a velocity dispersion of $\sigma_v = 4.7^{+1.5}_{-1.3}$ km s $^{-1}$ based on a two-component Gaussian mixture model (§4.1). If in equilibrium, this implies a dynamical mass of $\sim 5.9^{+3.8}_{-3.3} \times 10^5 M_\odot$ and a mass-to-light

ratio of $(M/L)_V = 660 \pm 600$. We opt for this approach to marginalize over the uncertainty in membership.

- From the 6 member stars with CaT-based [Fe/H] measurements, we measure $[\text{Fe}/\text{H}] = -2.45^{+0.13}_{-0.13}$ and $\sigma_{[\text{Fe}/\text{H}]} = 0.30^{+0.15}_{-0.11}$ dex (§4.2).
- We conclude that W1 is a dwarf galaxy based on its dynamical mass-to-light ratio (§4.1), observed metallicity spread (§4.2), lack of mass segregation within $\sim 1 r_{\text{half,ell}}$ (§5.2), and position on the size-luminosity plane (§7.1).
- The evidence for tidal disruption outweighs the evidence against tidal disruption (§7.2). While W1 is quite dense, we find that our best-fit orbital solution (§6.1) and comparison with our simulations of tidal streams (§6.2) indicate a sustained passage near the Milky Way over the course of its orbit. This history could explain the elliptical shape, asymmetric velocity distribution (§4.1), and offset on the luminosity-metallicity plane of W1. We thus conclude that the internal velocity dispersion of W1 is unlikely to accurately reflect the dynamical mass of the system. The true dynamical nature of W1 may be better understood through deeper wide-field imaging and spectroscopy as well as more detailed dynamical modeling to assess the validity and use of equilibrium models.

Looking ahead, the upcoming Vera C. Rubin Observatory’s Legacy Survey of Space and Time (LSST) is expected to uncover a population of similarly faint, distant, and low luminosity Local Group satellites. Many of these objects are likely to resemble W1, with sparse red giant branches, uncertain membership, and properties that blur the line between star clusters and dwarf galaxies. Fully taking advantage of these discoveries will require extensive spectroscopic follow-up in order to secure clean member samples for accurate kinematic and chemical measurements. By developing the tools needed to characterize these systems, we are better equipped to understand the satellites LSST will reveal and their place in the broader Local Group satellite population. From this, we can more comprehensively test our predictions of cosmological models and the processes that govern galaxy formation, evolution, and structure on the smallest scales.

ACKNOWLEDGMENTS

This research has made extensive use of the Keck Observatory Archive (KOA), which is operated by the W. M. Keck Observatory and the NASA Exoplanet Science Institute (NExScI), under contract with the National Aeronautics and Space Administration. We thank Ricardo Muñoz for making his raw Megacam photometric catalogs available.

This work has made use of data from the European Space

988 Agency (ESA) mission Gaia³, processed by the Gaia Data
 989 Processing and Analysis Consortium (DPAC⁴). Funding for
 990 the DPAC has been provided by national institutions, in par-
 991 ticular the institutions participating in the Gaia Multilateral
 992 Agreement.

993 **Software:** This research made use of many community-
 994 developed or community-maintained software packages, in-
 995 cluding (in alphabetical order): Astropy ([Astropy Collabora-](#)

996 [tion et al. 2013](#)), Emcee ([Foreman-Mackey et al. 2013](#)), gala
 997 ([Price-Whelan 2017](#)), galpy ([Bovy 2015](#)), IPython ([Perez
 998 & Granger 2007](#)), Jupyter ([jupyter.org](#)), Matplotlib ([Hunter
 999 2007](#)), NumPy ([van der Walt et al. 2011](#)), pandas ([McKin-
 1000 ney 2010](#)), photutils ([Bradley et al. 2025](#)), SciPy ([Jones et al.
 1001 2001](#)). This research has also made use of NASA’s Astro-
 1002 physics Data System.

1003 **Facility:** Gaia, Keck:II (DEIMOS)

REFERENCES

- 1004 Aliu E., et al., 2009, [ApJ](#), **697**, 1299
 1005 Armstrong B. M., Bekki K., Ludlow A. D., 2021, [MNRAS](#), **500**, 2937
 1006 Astropy Collaboration et al., 2013, [A&A](#), **558**, A33
 1007 Battaglia G., Starkenburg E., 2012, [A&A](#), **539**, A123
 1008 Baumgardt H., Faller J., Meinholt N., McGovern-Greco C., Hilker M.,
 1009 2022, [MNRAS](#), **510**, 3531
 1010 Belokurov V., et al., 2007, [ApJ](#), **654**, 897
 1011 Binney J., Tremaine S., 1987.
 1012 Bovy J., 2015, [ApJS](#), **216**, 29
 1013 Bradley L., et al., 2025, astropy/photutils: 2.2.0,
 1014 doi:[10.5281/zenodo.14889440](#),
<https://doi.org/10.5281/zenodo.14889440>
 1015 Bressan A., Marigo P., Girardi L., Salasnich B., Dal Cero C., Rubele S.,
 1016 Nanni A., 2012, [MNRAS](#), **427**, 127
 1017 Bringmann T., Doro M., Fornasa M., 2009, [JCAP](#), **2009**, 016
 1018 Carrera R., Pancino E., Gallart C., del Pino A., 2013, [MNRAS](#), **434**, 1681
 1019 Cerny W., et al., 2024, arXiv e-prints, p. arXiv:2410.00981
 1020 Choi J., Dotter A., Conroy C., Cantiello M., Paxton B., Johnson B. D.,
 1021 2016, [ApJ](#), **823**, 102
 1022 Collins M. L. M., Tollerud E. J., Rich R. M., Ibata R. A., Martin N. F.,
 1023 Chapman S. C., Gilbert K. M., Preston J., 2020, [MNRAS](#), **491**, 3496
 1024 Correa Magnus L., Vasiliev E., 2022, [MNRAS](#), **511**, 2610
 1025 D’Souza R., Bell E. F., 2022, [MNRAS](#), **512**, 739
 1026 Dey A., et al., 2019, [AJ](#), **157**, 168
 1027 Dotter A., 2016, [ApJS](#), **222**, 8
 1028 Drlica-Wagner A., et al., 2015, [ApJ](#), **813**, 109
 1029 Durbin M. J., et al., 2025, arXiv e-prints, p. arXiv:2505.18252
 1030 Erkal D., et al., 2021, [MNRAS](#), **506**, 2677
 1031 Errani R., Peñarrubia J., Walker M. G., 2025, arXiv e-prints, p.
 1032 arXiv:2505.22717
 1033 Faber S. M., et al., 2003, in Instrument Design and Performance for
 1034 Optical/Infrared Ground-based Telescopes. Edited by Iye & Moorwood,
 1035 Proceedings of the SPIE, Volume 4841, pp. 1657.
 1036 Fardal M. A., Huang S., Weinberg M. D., 2015, [MNRAS](#), **452**, 301
 1037 Filion C., Wyse R. F. G., 2021, [ApJ](#), **923**, 218
 1038 Ford H. C., et al., 1998, in Bely P. Y., Breckinridge J. B., eds, Society of
 1039 Photo-Optical Instrumentation Engineers (SPIE) Conference Series Vol.
 1040 3356, Space Telescopes and Instruments V. pp 234–248,
 1041 doi:[10.1117/12.324464](#)
 1042 Foreman-Mackey D., Hogg D. W., Lang D., Goodman J., 2013, [PASP](#), **125**,
 1043 306
 1044 Fritz T. K., Battaglia G., Pawlowski M. S., Kallivayalil N., van der Marel
 1045 R., Sohn S. T., Brook C., Besla G., 2018, [A&A](#), **619**, A103
 1046 Fu S. W., et al., 2023, arXiv e-prints, p. arXiv:2306.06260
 1047 Gaia Collaboration et al., 2023, [A&A](#), **674**, A1
 1048 Geha M., et al., 2026, [ApJ](#), pp <https://doi.org/10.3847/1538-4357/ae290d>
 1049 Gullikson K., Dodson-Robinson S., Kraus A., 2014, [AJ](#), **148**, 53
 1050
 1051 Hernquist L., 1990, [ApJ](#), **356**, 359
 1052 Hinton S. R., Davis T. M., Lidman C., Glazebrook K., Lewis G. F., 2016,
 1053 [Astronomy and Computing](#), **15**, 61
 1054 Homma D., et al., 2024, [PASJ](#), **76**, 733
 1055 Hunter J. D., 2007, [Computing in Science Engineering](#), **9**, 90
 1056 Husser T. O., Wende-von Berg S., Dreizler S., Homeier D., Reiners A.,
 1057 Barman T., Hauschildt P. H., 2013, [A&A](#), **553**, A6
 1058 Innanen K. A., Harris W. E., Webbink R. F., 1983, [AJ](#), **88**, 338
 1059 Ji A. P., et al., 2021, [ApJ](#), **921**, 32
 1060 Jones E., Oliphant T., Peterson P., et al., 2001, SciPy: Open source
 1061 scientific tools for Python, <http://www.scipy.org/>
 1062 Kim D., Jerjen H., Milone A. P., Mackey D., Da Costa G. S., 2015, [ApJ](#),
 1063 **803**, 63
 1064 Kirby E. N., Boylan-Kolchin M., Cohen J. G., Geha M., Bullock J. S.,
 1065 Kaplinghat M., 2013a, [ApJ](#), **770**, 16
 1066 Kirby E. N., Cohen J. G., Guhathakurta P., Cheng L., Bullock J. S.,
 1067 Gallazzi A., 2013b, [ApJ](#), **779**, 102
 1068 Kirby E. N., Cohen J. G., Simon J. D., Guhathakurta P., 2015, [ApJL](#), **814**,
 1069 L7
 1070 Koposov S. E., Belokurov V., Torrealba G., Evans N. W., 2015, [ApJ](#), **805**,
 1071 130
 1072 Li S., Liang Y.-F., Fan Y.-Z., 2021, [PhRvD](#), **104**, 083037
 1073 Loewenstein M., Kusenko A., 2010, [ApJ](#), **714**, 652
 1074 Loewenstein M., Kusenko A., 2012, [ApJ](#), **751**, 82
 1075 Longeard N., et al., 2018, [MNRAS](#), **480**, 2609
 1076 Machado R. E. G., Tauil G. C., Schweder-Souza N., 2025, Accuracy of
 1077 analytic potentials for orbits of satellites around a Milky Way-like
 1078 galaxy: comparison with *N*-body simulations (arXiv:2506.13813),
 1079 <https://arxiv.org/abs/2506.13813>
 1080 Martin N. F., Ibata R. A., Chapman S. C., Irwin M., Lewis G. F., 2007,
 1081 [MNRAS](#), **380**, 281
 1082 Martin N. F., de Jong J. T. A., Rix H.-W., 2008, [ApJ](#), **684**, 1075
 1083 Martinez G. D., Minor Q. E., Bullock J., Kaplinghat M., Simon J. D., Geha
 1084 M., 2011, [ApJ](#), **738**, 55
 1085 Maxted P. F. L., Heber U., Marsh T. R., North R. C., 2001, [MNRAS](#), **326**,
 1086 1391
 1087 McDaniel A., Ajello M., Karwin C. M., Di Mauro M., Drlica-Wagner A.,
 1088 Sanchez-Conde M. A., 2023, arXiv e-prints, p. arXiv:2311.04982
 1089 McKinney W., 2010, in van der Walt S., Millman J., eds, Proceedings of the
 1090 9th Python in Science Conference. pp 51 – 56
 1091 Miyamoto M., Nagai R., 1975, [PASJ](#), **27**, 533
 1092 Muñoz R. R., Côté P., Santana F. A., Geha M., Simon J. D., Oyarzún G. A.,
 1093 Stetson P. B., Djorgovski S. G., 2018a, [ApJ](#), **860**, 65
 1094 Muñoz R. R., Côté P., Santana F. A., Geha M., Simon J. D., Oyarzún G. A.,
 1095 Stetson P. B., Djorgovski S. G., 2018b, [ApJ](#), **860**, 66
 1096 Navabi M., Carrera R., Noël N. E. D., Gallart C., Pancino E., De Leo M.,
 1097 2026, [MNRAS](#), **546**, stag019
 1098 Navarro J. F., Frenk C. S., White S. D. M., 1997, [The Astrophysical
 1099 Journal](#), **490**, 493
 1100 Nieto D., Mirabal N., 2010, arXiv e-prints, p. arXiv:1003.3745
 1101 Ou X., et al., 2024, [ApJ](#), **966**, 33
 1102 Pace A. B., 2025, [The Open Journal of Astrophysics](#), **8**, 142
 1103 Pace A. B., Erkal D., Li T. S., 2022, [ApJ](#), **940**, 136

³ <https://www.cosmos.esa.int/gaia>

⁴ <https://www.cosmos.esa.int/web/gaia/dpac/consortium>

- 1104 Patel E., Chatur L., Mao Y.-Y., 2024, *ApJ*, **976**, 171
 1105 Paust N. E. Q., et al., 2009, *AJ*, **137**, 246
 1106 Peñarrubia J., Navarro J. F., McConnachie A. W., Martin N. F., 2009, *ApJ*,
 1107 **698**, 222
 1108 Perez F., Granger B. E., 2007, *Computing in Science Engineering*, **9**, 21
 1109 Plummer H. C., 1911, *MNRAS*, **71**, 460
 1110 Price-Whelan A. M., 2017, *The Journal of Open Source Software*, **2**
 1111 Prochaska J. X., Hennawi J. F., Westfall K. B., Cooke R. J., Wang F., Hsyu
 1112 T., Farina E. P., 2020, arXiv e-prints, p. [arXiv:2005.06505](#)
 1113 Richstein H., et al., 2024, *ApJ*, **967**, 72
 1114 Rocha M., Peter A. H. G., Bullock J., 2012, *MNRAS*, **425**, 231
 1115 Saeedi S., Sasaki M., 2020, *MNRAS*, **499**, 3111
 1116 Schiavon R. P., Barbay B., Rossi S. C. F., Milone A. 1997, *ApJ*, **479**, 902
 1117 Schlegel D. J., Finkbeiner D. P., Davis M., 1998, *ApJ*, **500**, 525
 1118 Siegel M. H., Shetrone M. D., Irwin M., 2008, *AJ*, **135**, 2084
 1119 Simon J. D., 2018, *ApJ*, **863**, 89
 1120 Simon J. D., 2019, *ARA&A*, **57**, 375
 1121 Simon J. D., Geha M., 2007, *ApJ*, **670**, 313
 1122 Sirianni M., et al., 2005, *PASP*, **117**, 1049
 1123 Smith S. E. T., et al., 2024, *ApJ*, **961**, 92
 1124 Sohn S. T., et al., 2007, *ApJ*, **663**, 960
 1125 Stetson P. B., 1987, *PASP*, **99**, 191

APPENDIX

A. DETAILS OF STARS USED IN OUR ANALYSIS

1148 Table A1 present the properties of the 73 stars compos-
 1149 ing the union of the 57 stars in our member sample (§3.2;

- 1126 Stetson P. B., 1992, in Worrall D. M., Biemesderfer C., Barnes J., eds,
 1127 Astronomical Society of the Pacific Conference Series Vol. 25,
 1128 Astronomical Data Analysis Software and Systems I. p. 297
 1129 Torrealba G., et al., 2016, *MNRAS*, **463**, 712
 1130 Tripathi A., Panwar N., Sharma S., Kumar B., Rastogi S., 2023, *Journal of
 1131 Astrophysics and Astronomy*, **44**, 61
 1132 Walker M. G., Mateo M., Olszewski E. W., Bernstein R., Wang X.,
 1133 Woodroofe M., 2006, *AJ*, **131**, 2114
 1134 Weatherford N. C., Chatterjee S., Kremer K., Rasio F. A., 2020, *ApJ*, **898**,
 1135 162
 1136 Willman B., Strader J., 2012, *AJ*, **144**, 76
 1137 Willman B., et al., 2005, *AJ*, **129**, 2692
 1138 Willman B., et al., 2006, *arXiv e-prints*, pp [astro-ph/0603486](#)
 1139 Willman B., Geha M., Strader J., Strigari L. E., Simon J. D., Kirby E., Ho
 1140 N., Warrens A., 2011, *AJ*, **142**, 128
 1141 Wolf J., Martinez G. D., Bullock J. S., Kaplinghat M., Geha M., Muñoz
 1142 R. R., Simon J. D., Avedo F. F., 2010, *MNRAS*, **406**, 1220
 1143 van der Marel R. P., Kallivayalil N., 2014, *ApJ*, **781**, 121
 1144 van der Walt S., Colbert S. C., Varoquaux G., 2011, *Computing in Science
 1145 Engineering*, **13**, 22

1150 $P_{\text{mem}} > 0.5$) and the 66 stars used in our mixture model (§4.1;
 1151 $P_{\text{mem,nov}} > 0.1$, $r_{\text{half,ell}} < 3$, $\text{Var} \neq 1$). We refer the reader to
 1152 Geha et al. (2026) for a detailed discussion of the data reduc-
 1153 tion, where the full table of stars, including non-members, is
 1154 available in Table 4.

Table A1. Properties of all stars observed with Keck/DEIMOS used in our analysis.

RA	DEC	v	v_{err}	r_o	r_{err}	g_o	g_{err}	[Fe/H]	[Fe/H] _{err}	gaia_source_id	Var	P_{mem}	Sample
[deg]	[deg]	[km/s]	[km/s]	[mag]	[mag]	[mag]	[mag]	–	dex	–	–	–	–
162.468948	51.061775	-19.51	0.69	18.174	0.002	18.722	0.002	-2.52	0.12	835977180433181056	0	0.69	1
162.325325	51.038049	-6.49	0.80	18.184	0.002	18.726	0.002	-2.26	0.12	835971820314006528	1	0.75	1
162.282500	50.947306	-11.87	1.37	18.297	0.003	18.186	0.003	–	–	835970136686823040	–	0.58	1
162.304798	51.042393	-24.46	3.03	19.741	0.004	19.343	0.004	–	–	836722438863176448	1	0.66	1
162.322595	51.057162	-11.87	1.16	20.098	0.003	20.508	0.003	-2.43	0.15	836722473222915968	0	0.84	1
162.366000	51.062694	-13.42	1.82	20.376	0.004	20.750	0.004	-2.26	0.15	835977725893619712	0	0.85	1
162.175765	51.033622	-6.48	1.33	20.423	0.004	20.619	0.004	–	–	836722889836066048	1	0.50	1
162.292215	51.050069	-11.46	1.29	20.528	0.004	20.909	0.004	-2.50	0.15	836722404504886912	0	0.85	1
162.283675	51.040804	-9.97	0.97	20.535	0.004	20.974	0.004	-1.54	0.14	836722335783961216	0	0.80	1
162.316500	51.040611	-9.50	2.24	20.573	0.004	20.990	0.004	-2.16	0.18	835971816018616320	0	0.66	1
162.338160	51.058369	-12.89	1.80	20.836	0.005	21.170	0.004	–	–	835971854673199616	0	0.94	1
162.394109	51.044394	-64.30	1.96	20.869	0.005	21.290	0.005	–	–	835977416655970816	0	0.00	0
162.242158	51.048312	-6.74	1.77	20.911	0.007	21.400	0.008	–	–	836722198345008512	0	0.64	1
162.420118	51.061132	-15.91	1.75	20.964	0.014	21.235	0.012	–	–	835977588454665856	0	0.87	1
162.378920	51.061358	-15.15	2.88	20.979	0.006	21.268	0.005	–	–	835977691533881088	0	0.93	1
162.319792	51.067500	-17.51	2.14	20.999	0.006	21.324	0.005	–	–	836722546237412608	0	0.93	1
162.403433	51.064206	-10.79	3.05	21.055	0.006	21.238	0.005	–	–	835977588454666368	0	0.74	1
162.511994	51.042236	-13.00	2.47	21.278	0.007	21.655	0.006	–	–	–	0	0.66	1
162.379208	51.026111	-73.13	2.79	21.367	0.007	21.759	0.006	–	–	–	–	0.00	0
162.366913	51.058278	-8.43	6.41	21.407	0.007	21.560	0.006	–	–	–	0	0.87	1
162.241949	51.089481	-98.13	3.04	21.447	0.014	21.938	0.021	–	–	–	0	0.00	0
162.238041	51.042064	-12.68	3.64	21.455	0.008	21.656	0.007	–	–	–	0	0.99	1
162.366953	51.031068	-23.41	5.63	21.459	0.008	21.633	0.007	–	–	–	0	0.75	1

Table A1 continued

Table A1 (*continued*)

RA [deg]	DEC [deg]	v [km/s]	v_{err} [km/s]	r_o [mag]	r_{err} [mag]	g_o [mag]	g_{err} [mag]	[Fe/H] –	[Fe/H]_err dex	gaia_source_id –	Var –	P_{mem} –	Sample –
162.359704	51.054519	-8.05	2.75	21.484	0.008	21.678	0.006	–	–	–	0	0.90	1
162.302359	51.051564	-6.03	4.13	21.499	0.008	21.705	0.007	–	–	–	0	0.84	1
162.354492	51.047914	0.50	3.96	21.546	0.008	21.756	0.007	–	–	–	0	0.67	1
162.282017	51.029489	-8.58	5.55	21.563	0.008	21.756	0.007	–	–	–	0	0.95	1
162.464771	51.031205	-21.26	2.85	21.570	0.009	21.917	0.007	–	–	–	0	0.56	1
162.264208	51.013500	-3.26	7.06	21.580	0.009	21.650	0.006	–	–	–	–	0.53	1
162.394826	51.074534	-18.42	4.47	21.581	0.009	21.832	0.008	–	–	–	0	0.89	1
162.185092	51.035045	-8.09	3.40	21.583	0.009	21.797	0.007	–	–	–	1	0.93	1
162.373926	51.049573	-19.65	4.41	21.639	0.009	21.802	0.007	–	–	–	0	0.81	1
162.291466	51.015660	-6.23	6.02	21.677	0.010	21.838	0.008	–	–	–	0	0.87	1
162.296696	51.075076	-9.78	3.27	21.696	0.010	21.888	0.007	–	–	–	0	0.97	1
162.447350	51.059632	-7.81	6.17	21.725	0.009	21.964	0.008	–	–	–	0	0.92	1
162.365213	51.059138	-11.66	4.76	21.734	0.009	21.923	0.008	–	–	–	0	0.99	1
162.325230	51.054659	-3.68	10.09	21.755	0.010	21.847	0.007	–	–	–	–	0.65	1
162.354249	51.040333	-14.41	4.94	21.761	0.010	21.956	0.008	–	–	–	0	0.98	1
162.271601	51.028406	-9.53	4.68	21.818	0.011	21.954	0.008	–	–	–	–	0.84	1
162.340002	51.045885	-8.79	6.32	21.856	0.010	22.044	0.009	–	–	–	1	0.96	1
162.203083	51.054694	63.33	5.23	21.856	0.009	22.291	0.009	–	–	–	–	0.00	0
162.323368	51.045459	-18.42	5.28	21.876	0.011	22.069	0.008	–	–	–	0	0.92	1
162.412363	51.082570	-11.91	11.86	21.897	0.012	22.124	0.011	–	–	–	–	0.96	1
162.321028	51.072971	-21.50	13.57	21.987	0.011	22.245	0.009	–	–	–	–	0.87	1
162.339527	51.042982	-6.48	10.91	22.055	0.012	22.229	0.009	–	–	–	–	0.86	1
162.307555	51.006356	24.23	7.34	22.158	0.012	22.401	0.010	–	–	–	–	0.07	0
162.316976	51.049973	-13.64	7.03	22.164	0.013	22.333	0.010	–	–	–	–	0.88	1
162.362730	51.058374	-9.94	14.21	22.174	0.014	22.355	0.011	–	–	–	–	0.92	1
162.275000	51.047694	57.32	5.44	22.184	0.013	22.705	0.012	–	–	–	–	0.00	0
162.348617	51.051101	7.51	4.74	22.207	0.013	22.437	0.011	–	–	–	–	0.41	0
162.315558	51.022664	-29.34	5.03	22.221	0.014	22.521	0.011	–	–	–	–	0.50	0
162.261708	50.994500	-13.21	11.12	22.227	0.013	22.444	0.011	–	–	–	–	0.99	1
162.450711	51.030172	-15.70	5.60	22.325	0.015	22.605	0.011	–	–	–	–	0.90	1
162.481266	51.063726	-7.74	5.97	22.337	0.015	22.570	0.013	–	–	–	–	0.92	1
162.312299	51.048340	-0.75	5.33	22.418	0.016	22.638	0.013	–	–	–	0	0.70	1
162.191875	51.000000	-56.49	14.64	22.429	0.015	22.654	0.012	–	–	–	–	0.10	0
162.328879	51.081601	-28.43	13.10	22.488	0.016	22.679	0.013	–	–	–	–	0.66	1
162.306097	51.045456	-2.56	6.82	22.519	0.017	22.788	0.013	–	–	–	0	0.80	1
162.386316	51.074238	-17.77	7.54	22.522	0.017	22.795	0.013	–	–	–	–	0.94	1
162.440265	51.035796	-23.59	6.94	22.575	0.019	22.849	0.014	–	–	–	–	0.75	1
162.448494	51.034428	-16.27	10.24	22.625	0.020	22.883	0.014	–	–	–	–	0.98	1
162.295516	51.037286	-26.38	12.14	22.661	0.020	22.912	0.015	–	–	–	–	0.75	1
162.364937	51.033600	-32.65	6.73	22.676	0.020	22.881	0.015	–	–	–	0	0.40	0
162.341717	51.055025	-37.80	13.69	22.715	0.020	22.996	0.015	–	–	–	0	0.45	0
162.434987	51.050797	-28.43	2.07	22.831	0.023	23.016	0.017	–	–	–	–	0.43	0
162.292417	51.082694	50.93	10.37	22.866	0.020	23.345	0.021	–	–	–	–	0.00	0
162.281167	51.055618	8.72	8.25	22.886	0.023	23.255	0.018	–	–	–	–	0.37	0
162.269784	51.054666	-23.40	6.03	22.899	0.023	23.116	0.017	–	–	–	1	0.69	1
162.373104	51.062638	82.11	8.87	22.900	0.025	23.160	0.019	–	–	–	–	0.00	0
162.326000	51.059500	-24.76	9.18	22.922	0.024	23.142	0.018	–	–	–	–	0.66	1
162.227050	51.057953	-22.41	9.30	23.085	0.028	23.344	0.022	–	–	–	–	0.79	1

Table A1 *continued*

Table A1 (*continued*)

RA [deg]	DEC [deg]	v [km/s]	v_{err} [km/s]	r_o [mag]	r_{err} [mag]	g_o [mag]	g_{err} [mag]	[Fe/H] –	[Fe/H]_err dex	gaia_source_id –	Var –	P_{mem} –	Sample –
162.496122	51.048836	32.14	6.15	23.102	0.028	23.378	0.022	–	–	–	–	0.02	0
162.216547	51.040881	29.80	8.04	23.329	0.037	23.719	0.029	–	–	–	–	0.03	0